ELSEVIER

Contents lists available at ScienceDirect

Journal of Computational Physics

journal homepage: www.elsevier.com/locate/jcp



Order enhanced finite volume methods through non-polynomial approximation



Andrew J. Christlieb a, William A. Sands b, Hyoseon Yang c,*

- ^a Department of Computational Mathematics, Science and Engineering, Michigan State University, East Lansing, MI, 48824, United States
- b Center for Predictive Engineering and Computational Science, Oden Institute for Computational Engineering and Sciences, The University of Texas at Austin, Austin, TX, 78712, United States
- ^c Department of Mathematics, Kyung Hee University, Seoul, 02447, South Korea

ARTICLE INFO

Article history: Received 9 July 2022 Received in revised form 16 December 2022 Accepted 19 January 2023 Available online 31 January 2023

Keywords:
Finite volume methods
Optimal order
Radial basis functions
WENO
Conservation laws
Shape parameter

ABSTRACT

In this paper, we introduce an approximation method that establishes certain order enhancements by leveraging radial basis functions (RBFs) in the numerical solution of conservation laws. The use of RBFs for interpolation and approximation is a well developed area of research. Of particular interest in this work is the development of high order finite volume (FV) weighted essentially non-oscillatory (WENO) methods, which utilize RBF approximations to obtain required data at cell interfaces. The aforementioned improvement in the order of accuracy is addressed through an analysis of the truncation error, resulting in expressions for the shape parameters appearing in the basis. This paper seeks to address the practical elements of the approach, including the evaluations of shape parameters as well as a hybrid implementation. To highlight the effectiveness of the non-polynomial basis in shock-capturing, the proposed methods are applied to systems of one-dimensional hyperbolic and weakly hyperbolic conservation laws and compared with several wellknown WENO schemes in the literature. We also include a two-dimensional example for a scalar problem that demonstrates an extension to multiple dimensions. In the case of the non-smooth, weakly hyperbolic test problem, notable improvements are observed in predicting the location and height of the finite time blowup. The numerical results demonstrate that the proposed schemes attain notable improvements in accuracy, as indicated by the analysis of the reconstructions. A key contribution of this work is the development of robust third-order WENO method, which further demonstrates the effectiveness of the non-polynomial basis.

© 2023 Elsevier Inc. All rights reserved.

1. Introduction

This work concerns the development of numerical schemes to solve conservation laws, which are of the form

$$\begin{cases} u_t + \nabla \cdot F(u) = 0, & x \in \mathbb{R}^m, \\ u(x, 0) = u_0(x), \end{cases}$$
 (1)

E-mail addresses: christli@msu.edu (A.J. Christlieb), william.sands@austin.utexas.edu (W.A. Sands), hyoseon@khu.ac.kr (H. Yang).

^{*} Corresponding author.

Table 1 Commonly used global radial basis functions ϕ with a shape parameter λ .

RBFs	$\phi(x)$
Gaussian function	$e^{-(\lambda x)^2}$
Multiquadric	$\sqrt{1+(\lambda x)^2}$
Inverse quadric	1
Thin-plate spline	$ \begin{array}{l} 1 + (\lambda x)^2 \\ (\lambda x)^2 \log(\lambda x) \end{array} $

where F(u) is the flux function and $u_0(x)$ is the prescribed initial data. The significance of the problem (1) has motivated, to a large extent, the development of numerous high-order numerical methods. In this way, our paper seeks to develop high order schemes for conservation laws by leveraging features endowed through a non-polynomial basis. The resulting methods demonstrate enhanced rates of convergence, which will be discussed throughout the paper.

Finite volume (FV) schemes are among the most popular methods used to solve hyperbolic conservation laws. An attractive feature of such schemes is that they evolve cell average data, which makes the discretization naturally conservative. These conservation properties also make them suitable for use in, for example, adaptive mesh refinement algorithms, where data needs to be frequently transferred between levels within a hierarchy of grids. The use of cell average data, rather than point-wise values, greatly simplifies the task of making such transfers conservative. While there exist many approaches to obtain high order FV discretizations, we restrict our focus to the class of so-called weighted ENO (WENO) schemes [26,28], developed by Jiang and Shu [26], which shall be referred to as classical WENO or WENO-IS. These methods were built on the success, and, in a sense, the limitations of the essentially non-oscillatory (ENO) schemes [19,20,37,38], which employed an adaptive interpolation stencil on a small set of available candidate points, to construct approximations at cell interfaces. WENO approaches, such as [26], in contrast, make use of all available candidate points in the reconstruction through a convex combination of substencils, so that higher order accuracy is recovered in smooth regions. In non-smooth regions, WENO reduces to making use of one of the substencils to obtain a properly winded, essentially non-oscillatory approximation. The notion of smoothness among each of the candidate substencils is assessed through a smoothness indicator that makes use of the first and second derivative information to identify non-smooth regions. Several other WENO schemes, which are more robust at shock-capturing and generate less dissipation, have been proposed in the literature (see e.g., [1,5,21,35]). Traditional WENO schemes were originally based on polynomial interpolation; however, algebraic polynomials are known to have limits in approximating data containing steep gradients or rapid variations due to their shift-and-scale invariant property. In order to address this problem, schemes were developed based on both trigonometric [48,49] and exponential [16,18] functions in the interpolation basis for ENO and WENO.

This paper proposes to use non-polynomial function approximations by formulating a WENO scheme in terms of RBFs and achieving enhanced convergence order by tuning the available shape or tension parameter. RBFs are widely used as a basis function for multivariate scattered data approximation problems [8,29,47], and RBF approximation methods for solving partial differential equations have been developed in a variety of contexts [34,41], including WENO quadratures [4,15]. A radial basis function $\phi: \mathbb{R}^d \to \mathbb{R}$ is defined in the sense that $\phi(x) = \phi(|x|)$, where $|\cdot|$ is the usual Euclidean norm. Because of its definition, the power of the RBF approximation is in its meshless property, which is particularly beneficial in modeling scattered data. Moreover, the basis is flexible, as it can be tuned to incorporate local features of the data through the shape parameter. For a given data set, an approximating function Af(x) with an RBF ϕ can be represented as

$$Af(x) = \sum_{i=1}^{M} \alpha_j \phi(|x - \xi_j|)$$
(2)

where $\{\xi_j: j=1,\cdots,M\}$ is a set of reference points and α_j is a weight associated with $\phi(\cdot-\xi_j)$ for $j=1,\cdots,M$. There are several ways to solve (2) depending on the constraints. For example, assuming $f(\Omega)$ is given, then the constraints satisfy

$$Af(x^*) = f(x^*), \quad \forall x^* \in \Omega, \tag{3}$$

which may represent the solution of an interpolation problem (if $|\Omega| = M$) or an optimization problem ($|\Omega| \neq M$). In Table 1, we provide commonly used global radial basis functions ϕ with a shape parameter λ . We note that the RBF approximation scheme (2) using a Gaussian function as a basis, i.e., $\phi(x) = e^{-(\lambda x)^2}$, has a conceptual resemblance with Gaussian Process (GP) modeling, which makes a probabilistic prediction instead of solving a linear system (3). In [30,31], the authors use GP regression to solve hyperbolic conservation laws.

The topic of order enhancing methods admits a vast array of literature. For example, several studies have explored the notion of superconvergence, with discontinuous Galerkin (DG) methods, on time evolution in ordinary differential equations [2,3], as well as hyperbolic and convection-diffusion PDEs [10,11,9,45]. In DG schemes, superconvergent behavior can be incorporated into the basis by using information from the exact solution, provided one is available. Spectral methods for PDEs can also achieve high order accuracy, when the solutions are analytic, for continuous problems. For PDEs that admit

discontinuous solutions, the Gibbs phenomenon is known to contaminate solutions, resulting in non-uniform convergence [12]. However, in such instances, high order accuracy can be recovered through the use of certain post-processing techniques [32,33,13,39]. In the literature, non-polynomial based numerical schemes have successfully demonstrated improvements in accuracy. We refer the interested readers to the papers [15] and [17]. The latter work develops a WENO scheme with a basis consisting of exponential polynomials, while the former proposes an ENO scheme that uses RBF interpolation. Moreover, in recent work, RBF-ENO methods have been successfully applied to problems on unstructured meshes [23–25]. The primary objective of this paper is to devise high order FV schemes using compact, non-polynomial interpolation techniques, which achieve additional accuracy by exploiting the shape parameter available in the basis. As will be discussed in section 3, the convergence order of the scheme is related to the level of accuracy of the approximation for shape parameter λ^2 , which appears in the basis, e.g., $\phi(x) = e^{-(\lambda x)^2}$.

The organization of this paper is as follows. In section 2, we begin with a general overview of RBF interpolation. Once we have introduced the interpolation problem, we demonstrate, in section 3, how the shape parameter in the basis can be exploited to obtain order enhanced convergent approximations. Then, in section 4, we briefly summarize the construction of FV WENO schemes for conservation laws, highlighting, in particular, subsection 4.2, which defines the smoothness indicators employed by the proposed schemes. We then outline the key steps used in the implementation of the algorithms in section 5, which also contains details concerning extensions for two-dimensional problems. Experimental results, collected on a suite of test problems consisting of one-dimensional hyperbolic and weakly hyperbolic systems of conservation laws, as well as a two-dimensional nonlinear scalar test problem, are presented in section 6. Finally, in section 7, we summarize the ideas presented in this work.

2. RBF interpolation

In this section, we provide a brief overview of interpolation with radial basis functions, which shall be useful for introducing our new WENO formulation. Suppose that a continuous function $f: \mathbb{R}^d \to \mathbb{R}$ is known only at a set of discrete points $X := \{x_1, ..., x_N\}$ in $\Omega \subset \mathbb{R}^d$. A function $\phi: \mathbb{R}^d \to \mathbb{R}$ is radial in the sense that $\phi(x) = \phi(|x|)$, where $|\cdot|$ is the usual Euclidean norm. RBF interpolation for f on X starts by choosing a basis function ϕ , and then defines an interpolant by

$$Af_X(x) := \sum_{k=1}^{m} \beta_k p_k(x) + \sum_{i=1}^{N} \alpha_i \phi(x - x_i),$$
(4)

where $\{p_1, \ldots, p_m\}$ is a basis for Π_m and the coefficients α_j and β_i are chosen to satisfy the linear system

$$\begin{cases}
Af_X(x_i) = \sum_{k=1}^m \beta_k p_k(x_i) + \sum_{j=1}^N \alpha_j \phi(x_i - x_j) = f(x_i), & i = 1, \dots, N, \\
\sum_{j=1}^N \alpha_j p_k(x_j) = 0, & k = 1, \dots, m.
\end{cases} (5)$$

Here Π_m denotes the space generated by all algebraic polynomials of degree less than m on \mathbb{R}^d . For a wide choice of functions ϕ and polynomial orders m, the existence and uniqueness of the solution of the linear system (5) is ensured when ϕ is a conditionally positive definite function.

Definition 2.1. Let $\phi: \mathbb{R}^d \to \mathbb{R}$ be a continuous function. We say that ϕ is conditionally positive definite of order $m \in \mathbb{N}$ if for every finite set of pairwise distinct points $X = \{x_1, \dots x_N\} \subset \mathbb{R}^d$ and $\alpha = (\alpha_1, \dots, \alpha_N) \in \mathbb{R}^N \setminus \{0\}$ satisfying $\sum_{j=1}^N \alpha_j p(x_j) = 0$ for $\forall p \in \Pi_m$, the quadratic form

$$\sum_{i=1}^{N} \sum_{j=1}^{N} \alpha_i \alpha_j \phi(x_i - x_j)$$

is positive definite.

This leads to the linear system (5) for $\alpha = (\alpha_1, \dots, \alpha_N)$ and $\beta = (\beta_1, \dots, \beta_m)$, which is given in block-matrix form as

$$\begin{bmatrix} \Phi & P^T \\ P & O \end{bmatrix} \begin{bmatrix} \alpha^T \\ \beta^T \end{bmatrix} = \begin{bmatrix} \mathbf{f}^T \\ O \end{bmatrix} \tag{6}$$

where $\Phi = \{\phi(x_i - x_j) : i, j\}$, $P = \{p_k(x_j) : k, j\}$ and $\mathbf{f} = \{f(x_i) : i\}$. If we assume m = 0 in (4), then from the equations (4) and (6), the interpolant can be represented as

$$Af_X(x) = \sum_{i=1}^N \alpha_j \phi(x - x_j) = \Phi^{-1} \mathbf{f}^T, \tag{7}$$

where $\phi = \{\phi(x - x_j) : j\}$. We note that the product $\phi \Phi^{-1}$, which appears as part of the representation (7), is completely independent of the function values **f**. Next, in section 3, expressions for the optimal shape parameters, i.e., λ^2 in the non-polynomial basis, are derived, which results in order enhancing approximations.

3. Order enhancing RBF schemes

In this section, we derive the expressions for optimal shape, or tension, parameters made available through RBF interpolation. We perform our analysis in section 3.1 based on two reconstruction methods: a direct approach using integrals and a second approach that utilizes a primitive function. Here, we define the shape parameter λ^2 , for a given RBF ϕ , so that it maximizes the convergence order of the approximation. Once the techniques have been demonstrated, we generalize these results in sections 3.2 and 3.3, with the key points summarized in Theorems 3.1 and 3.3, respectively.

3.1. Optimal shape parameters for RBFs

In [16], the authors introduced a WENO scheme based on the space of exponential polynomials. Later, in the work [18], they improved the order of accuracy of their schemes by exploiting the control parameter $\lambda \in \mathbb{R}$ or $i\mathbb{R}$ for exponential basis functions of the form $e^{\lambda x}$. We adopt a similar strategy in this work with the difference being the choice of the basis. Here, the basis functions consist of infinitely smooth RBFs ϕ (see Table 1) rather than exponential polynomials. We present the analysis using the Gaussian function

$$\phi(x) = e^{-\lambda^2 x^2}, \quad \lambda \in \mathbb{R} \text{ or } i\mathbb{R}, \tag{8}$$

in the case of N = 2, using two different approaches, but these techniques can be easily extended to other RBFs (see Table 1 for other options). For each approach, we provide analytical expressions for the optimal shape parameters, which allow the schemes to achieve optimal convergence order on a fixed reconstruction stencil.

3.1.1. Direct computation with integrals

Recall that the RBF approximation is given by

$$Au(x) := \sum_{k=1}^{2} \alpha_k \phi(x - x_{j+k-1}) = \alpha_1 \phi(x - x_j) + \alpha_2 \phi(x - x_{j+1}).$$
(9)

The goal is to form a high order approximation using the form (9), which preserves each of the cell averages. In other words, the approximation should satisfy the integral constraint

$$\frac{1}{\Delta x} \int_{I_i} Au(\xi) d\xi = \bar{u}_i, \quad i = j, \ j + 1. \tag{10}$$

Using the RBF $\phi(x)$ defined in (8), it follows that the integrals of ϕ can be evaluated analytically, which resulting in a solvable linear system. Once the solution is determined, the final approximation at the cell boundary $x_{j+\frac{1}{3}}$ is given by

$$Au(x_{j+\frac{1}{2}}) = \frac{2\lambda\Delta x \exp(-\frac{\lambda^2 \Delta x^2}{4})}{\sqrt{\pi} \left(\operatorname{erf}(\frac{\lambda\Delta x}{2}) + \operatorname{erf}(\frac{3\lambda\Delta x}{2}) \right)} (\bar{u}_j + \bar{u}_{j+1}).$$

To determine the shape parameter, we Taylor expand the right-hand side of the previous equation, which yields

$$\begin{split} Au(x_{j+\frac{1}{2}}) &\approx \left(\frac{1}{2} + \frac{\lambda^2 \Delta x^2}{6} - \frac{7\lambda^4 \Delta x^4}{90}\right) (\bar{u}_j + \bar{u}_{j+1}) \\ &= u(x_{j+\frac{1}{2}}) + \Delta x^2 \left(\frac{1}{3}\lambda^2 u(x_{j+\frac{1}{2}}) + \frac{1}{6}u''(x_{j+\frac{1}{2}})\right) + \mathcal{O}(\Delta x^4). \end{split}$$

Hence, we have a second order approximation for the cell boundary point. Notice that we can obtain a fourth order approximation if we choose the shape parameter with

$$\lambda^{2} = -\frac{u''(x_{j+\frac{1}{2}})}{2u(x_{j+\frac{1}{2}})} + \mathcal{O}(\Delta x^{2}).$$

In practice, this parameter can be formed entirely from the available cell average data. Although there may be many ways to approximate these terms, our implementation considers finite difference approximations to the derivatives appearing in the expression for the optimal shape parameter. We provide additional details in Appendix A. Note that the cell average data can be shifted by some positive constant at the beginning and end of the reconstruction steps to prevent division by zero, if needed. In the next section, we perform a similar reconstruction using a primitive function.

3.1.2. Construction with a primitive function

To reconstruct the approximation at the cell boundary $x = x_{j+\frac{1}{2}}$ from the cell averages $\{\bar{u}_j, \bar{u}_{j+1}\}$, we define a primitive function

$$U(x) = \int_{x_{i-\frac{1}{2}}}^{x} u(\xi)d\xi$$

which can be explicitly written in terms of the available cell averages as

$$U(x_{i-\frac{1}{2}}) = \Delta x \sum_{\ell=i}^{i-1} \bar{u}_{\ell}$$
 for $i = j, \dots, j+2$.

Using the available interpolatory data for the primitive function at the cell interfaces, we seek an RBF representation

$$AU(x) := \sum_{k=0}^{2} \alpha_k \phi\left(x - x_{j+k-\frac{1}{2}}\right),\tag{11}$$

which satisfies

$$AU(x_{i-\frac{1}{2}}) = U(x_{i-\frac{1}{2}}), \quad i = j, j+1, j+2.$$
 (12)

Then the final approximation to u(x) at $x = x_{i+\frac{1}{2}}$ is obtained by differentiating the RBF representation

$$AU'(x) := \sum_{k=0}^{2} \alpha_k \phi'(x - x_{j+k-\frac{1}{2}}),$$

which approximates U'(x) = u(x), i.e.,

$$AU'(x_{i+\frac{1}{2}}) \approx U'(x_{i+\frac{1}{2}}) = u(x_{i+\frac{1}{2}}). \tag{13}$$

The approximation with a Gaussian RBF $\phi(x)$ is found to be

$$AU'(x_{j+\frac{1}{2}}) = 2\lambda^2 \Delta x^2 \frac{e^{3\lambda^2 \Delta x^2}}{e^{4\lambda^2 \Delta x^2} - 1} (\bar{u}_j + \bar{u}_{j+1}), \tag{14}$$

with the basis coefficients calculated from (12) and (13). Applying a Taylor expansion to the right-hand side of this equation gives

$$\begin{split} AU'(x_{j+\frac{1}{2}}) &\approx \left(\frac{1}{2} + \frac{1}{2}\lambda^2 \Delta x^2 - \frac{1}{12}\lambda^4 \Delta x^4\right)(\bar{u}_j + \bar{u}_{j+1}) \\ &= u(x_{j+\frac{1}{2}}) + \Delta x^2 \left(\lambda^2 u(x_{j+\frac{1}{2}}) + \frac{1}{6}u''(x_{j+\frac{1}{2}})\right) + \mathcal{O}(\Delta x^4). \end{split}$$

Hence, we have the second order approximation for the reconstructed cell boundary point. Alternatively, we can obtain the fourth order approximation if we choose the shape parameter with

$$\lambda^{2} = -\frac{u''(x_{j+\frac{1}{2}})}{6u(x_{j+\frac{1}{2}})} + \mathcal{O}(\Delta x^{2}), \tag{15}$$

which can be computed using the techniques explained at the end of section 3.1.1 and further described in Appendix A. Using this same machinery, we can generalize these approximations by considering the parity of N, which results in two theorems, which seek to address the overall convergence order.

3.2. Three-point RBF schemes

Following the analysis of the previous section, we construct RBF interpolation schemes with optimal parameters when the number of the stencil points N is odd. Through a fairly direct construction, one obtains the following theorem:

Theorem 3.1. Let u be a smooth function on Ω and ϕ be a smooth radial basis function. Given a set of reference points $\{x_k \in \Omega : k = 1, \dots, N\}$ for an odd integer N, there exists a set of coefficients $\{\alpha_k : k = 1, \dots, N\}$ of the approximation

$$Au(x) = \sum_{k=1}^{N} \alpha_k \phi(x - x_k)$$

to the function u(x), which are constructed from cell averaged data $\{\bar{u}(x_j): x_j \in \Omega\}$. Furthermore, the approximation can be made (N+1)st order accurate. i.e.,

$$Au(x) = u(x) + \mathcal{O}(\Delta x^{N+1}),$$

for $x \in \Omega$.

We show an example for the case of N=3 on behalf of the proof of Theorem 3.1. Suppose that we construct the approximation of a smooth function u at $x=x_{j+\frac{1}{n}}$ using the cell averages $\{\bar{u}_j: j=-1,0,1\}$. Using a primitive function

$$U(x) = \int_{x_{j-\frac{1}{2}}}^{x} u(\xi)d\xi,$$

the approximation using a radial basis function $\phi(x) = e^{-\lambda^2 x^2}$ is defined by

$$AU(x) := \sum_{k=-1}^{2} \alpha_k \phi(x - x_{j+k-\frac{1}{2}}),$$

so that $AU'(x) \approx u(x)$. Repeating the steps outlined in subsection 3.1.2, and Taylor expanding the RBF approximation, we find that

$$AU'(x_{j+\frac{1}{2}}) = u(x_{j+\frac{1}{2}}) + \Delta x^3 \left(\lambda^2 u'(x_{j+\frac{1}{2}}) + \frac{1}{12} u'''(x_{j+\frac{1}{2}}) \right) + \mathcal{O}(\Delta x^4).$$

Therefore the third order scheme can be improved to fourth order accuracy through the choice

$$\lambda^2 = -\frac{u'''(x_{j+\frac{1}{2}})}{12u'(x_{j+\frac{1}{2}})} + \mathcal{O}(\Delta x),\tag{16}$$

which can be computed using the same techniques discussed in Appendix A.

Remark 3.2. Following the brief discussion in Appendix A, the approximation (16) requires one additional cell average value that lies outside of the three-point global reconstruction stencil for $u_{j+\frac{1}{2}}^-$. Since the derivatives in this approximation do not need to be winded, this cell average value can be selected to lie in the union of global reconstruction stencils used to form $u_{j+\frac{1}{2}}^-$ and $u_{j+\frac{1}{2}}^+$, i.e., $\{\bar{u}_{j-1}, \bar{u}_j, \bar{u}_{j+1}, \bar{u}_{j+2}\}$. This is identical to the stencil used by the third order WENO-JS scheme when forming the flux at $x_{j+1/2}$.

3.3. Four-point RBF schemes

Here we provide the following theorem for the case when *N* is even to complete the analysis of proposed scheme. Again, through a fairly straightforward construction, one obtains the general theorem, which is as follows:

Theorem 3.3. Let u be a smooth function on Ω and ϕ is a smooth radial basis function. Given a set of reference points $\{x_k \in \Omega : k = 1, \dots, N\}$ for an even integer N, there exists a set of coefficients $\{\alpha_k : k = 1, \dots, N\}$ of the approximation

$$Au(x) = \sum_{k=1}^{N} \alpha_k \phi(x - x_k)$$

to the function u(x), which are constructed from cell averaged data $\{\bar{u}(x_j): x_j \in \Omega\}$. Moreover, the resulting approximation is (N+p)th order accurate, with 0 , i.e.,

$$Au(x) = u(x) + \mathcal{O}(\Delta x^{N+p}),$$

for $x \in \Omega$.

Here, we provide the analysis for the case N=4. Using the cell averages $\{\bar{u}_j: j=-1,\cdots,2\}$, the approximation is defined by

$$AU(x) := \sum_{k=-1}^{3} \alpha_k \phi(x - x_{j+k-\frac{1}{2}})$$
(17)

and at the cell boundary $x = x_{j+\frac{1}{2}}$, we have that

$$AU(x_{i-\frac{1}{2}}) = U(x_{i-\frac{1}{2}})$$

$$= \Delta x \sum_{\ell=i}^{i-1} \bar{u}_{\ell}, \quad i = j-1, \dots, j+3.$$
(18)

Proceeding as before, we can obtain the solution

$$AU'(x_{j+\frac{1}{2}}) \approx \sum_{k=-1}^{2} C_k \bar{u}_{j+k} \tag{19}$$

with coefficients C_k computed from equations (17) and (18). As before, these can be Taylor expanded about the cell boundary $x = x_{i+\frac{1}{2}}$ and we find that

$$AU'(x_{j+\frac{1}{2}}) = u(x_{j+\frac{1}{2}}) + \Delta x^4 \left(\frac{1}{30}u^{(4)}(x_{j+\frac{1}{2}}) + \frac{2}{3}\lambda^2 u''(x_{j+\frac{1}{2}}) + 2u(x_{j+\frac{1}{2}})\lambda^4\right) + \mathcal{O}(\Delta x^6).$$

Next, we choose λ^2 to remove the $\mathcal{O}(\Delta x^4)$ term, i.e.,

$$\lambda^{2} = \frac{-\frac{1}{3}u''(x_{j+\frac{1}{2}}) \pm \sqrt{\frac{1}{9}u''(x_{j+\frac{1}{2}})^{2} - \frac{1}{15}u(x_{j+\frac{1}{2}})u^{(4)}(x_{j+\frac{1}{2}})}}{2u(x_{j+\frac{1}{2}})} + \mathcal{O}(\Delta x^{p}), \tag{20}$$

which can be computed using the same techniques discussed in Appendix A. Therefore we can obtain a optimal scheme, which is (4 + p)th order accurate with $p \le 2$. We now proceed to the discussion of WENO schemes in section 4, making use of the RBF approximations.

Remark 3.4. In contrast to Remark 3.2, evaluating the approximation (20), with p=2, requires one additional cell average value that lies outside of the union of global reconstruction stencils, in the fifth order WENO-JS scheme, to compute $u_{j+\frac{1}{2}}^-$ and $u_{j+\frac{1}{2}}^+$. On the other hand, when p=1, the "effective stencil" is no larger than the global stencil used by the fifth order WENO-JS scheme in the construction of the flux at $x=x_{j+\frac{1}{2}}$.

4. WENO schemes

This section describes the general formulation of FV WENO schemes used to solve conservation laws. First, we provide a brief summary of the FV discretization in section 4.1. Then, in section 4.2, we introduce new smoothness indicators, which were motivated by numerical experimentation, and discuss the mapping for the WENO weights.

4.1. Formulation of a finite volume scheme

Consider one-dimensional variant of (1), which takes the form

$$u_t + f(u)_x = 0, \quad x \in \mathbb{R},$$

 $u(x, 0) = u_0(x).$ (21)

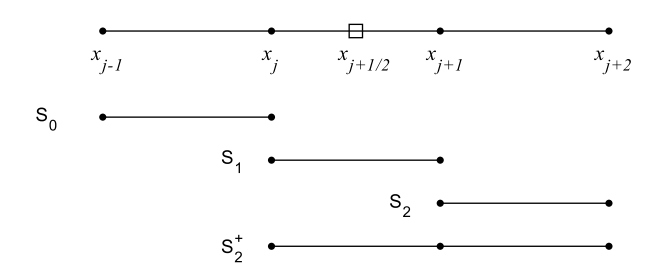


Fig. 1. Three two-point substencils S_k , k = 0, 1, 2 and a three-point substencil S_2^+ .

To develop a FV discretization, we let the computational domain be partitioned into uniform cells, so that the jth cell is given by $I_j = [x_{j-1/2}, x_{j+1/2}]$. Further, since the cells are uniformly spaced, each has the size $\Delta x = x_{j+1/2} - x_{j-1/2}$. FV schemes require cell averages of the solution u

$$\bar{u}_j(t) := \frac{1}{\Delta x} \int_{I_j} u(x, t) dx,\tag{22}$$

where the integrals in (22) can be numerically approximated through quadrature of suitable accuracy. By integrating the (21) over the control volume I_i , one obtains a collection of evolution equations defined in each of the control volumes, i.e.,

$$\frac{d}{dt}\bar{u}_{j}(t) = -\frac{1}{\Delta x} \left(f(u(x_{j+1/2})) - f(u(x_{j-1/2})) \right). \tag{23}$$

Defining the numerical flux $\hat{f}_{j\pm 1/2}$ by

$$\hat{f}_{j\pm 1/2} = h(u_{j\pm 1/2}^-, u_{j\pm 1/2}^+), \tag{24}$$

the equation (23) is approximated as

$$\frac{d}{dt}\bar{u}_{j}(t) = -\frac{1}{\Delta x} \left(\hat{f}_{j+1/2} - \hat{f}_{j-1/2} \right). \tag{25}$$

The monotone flux h satisfies several properties, namely, it is Lipschitz continuous in both arguments and should be consistent with the physical flux f, i.e., h(u,u)=f(u). Moreover, the flux should be non-decreasing (non-increasing) with respect to the first (second) argument. In this paper, we employ the HLLC and Lax-Friedrichs fluxes for solving the hyperbolic problems and a Godunov flux for the weakly hyperbolic system. The definitions of these numerical fluxes can be found in section 6. Next, we focus on the WENO component of the proposed schemes, which seeks to develop high order reconstructions for the cell average data supplied to the numerical flux functions, i.e., $u_{j\pm 1/2}^-$ and $u_{j\pm 1/2}^+$.

4.2. Construction of new smoothness indicators for WENO-RBF schemes

It is well known that the smoothness indicator plays a pivotal role in the WENO reconstruction procedure. We are proposing a three-point WENO scheme and a four-point WENO scheme based on RBFs with optimal parameters, so it will be helpful to introduce some references to simplify names for the schemes. From now on, we shall refer to the three-point and four-point WENO schemes, which are based on RBFs, as WENO-RBF3 and WENO-RBF4, respectively. Furthermore, the WENO-RBF3 scheme is constructed using two two-point substencils (S_0 , S_1 in Fig. 1), while the WENO-RBF4 scheme is using three two-point substencils (S_0 , S_1 , S_2 in Fig. 1) so that only the first-order difference operator can be used to estimate the smoothness of numerical fluxes. In other words, the small size of the substencils, used by the RBF methods, introduces limitations which make capturing highly oscillatory structures and rapid gradients challenging, especially on coarse grids.

In an effort to amend this issue, we employ difference operators which have so-called *exponentially vanishing moments*. The basic idea is that difference operators are constructed so that their applications to smooth functions result in more rapid convergence to zero than classical undivided differences. Before proceeding, we first introduce some ideas from a recent work [17], in which smoothness indicators were constructed using exponential polynomials.

Consider a smooth function f. Exponential polynomials can be characterized as the kernel of an operator $p_m(D)$ of the form

$$p_m(D)[f] := \prod_{i=1}^m (D - \gamma_i I)[f], \tag{26}$$

where D is a continuous differential operator, I is an identity operator and $\gamma_i \in \mathbb{C}$, which is associated with the target exponential polynomials. Then, the operator $p_m(D)$ is constructed as a differential operator which annihilates exponential

polynomials. For our purposes, it suffices to consider the case m=1 in equation (26). To illustrate, consider an exponential function $g(x) = e^{-\gamma x}$ for some constant γ and the first order operator $p_1(D)$ with the form

$$p_1(D)[f] = (D + \gamma I)[f].$$

Then this operator annihilates the exponential function g, i.e.,

$$p_1(D)[g](x) = D[g](x) + \gamma g(x) = -\gamma e^{-\gamma x} + \gamma e^{-\gamma x} = 0.$$

For the discretized version, we assume that the function values $\{f(x_{i-1}), f(x_i)\}$ of a smooth function f on the stencil $\{x_{i-1}, x_i\}$ are available with $\Delta x = x_i - x_{i-1}$. Then, the discrete version operator $\mathbf{p}_1(D)$ of continuous $p_1(D)$ at x_i is defined as

$$\mathbf{p}_1(D)_i[f] := (D + \gamma I)_i[f] := e^{\gamma \Delta x} f(x_i) - f(x_{i-1}),$$

which also annihilates the exponential function, i.e.,

$$\mathbf{p}_1(D)_i[g] = e^{\gamma \Delta x} e^{-\gamma x_i} - e^{-\gamma x_{i-1}} = 0,$$

for $g(x) = e^{-\gamma x}$. Here we say the operators $p_1(D)$ and $\mathbf{p}_1(D)_i$ have the exponential vanishing moments and such operators should be more effective at detecting smoothness, or lack thereof, in the data, even on a small collection of points than classical differential operator. Similar constructions can be achieved for $m \ge 2$, leading to mth order operators, which annihilate m exponential polynomials. For additional information, we refer interested readers to [17].

We are now ready to propose new smoothness indicators based on the new undivided difference with exponentially vanishing moments. Specifically, we define β_k , k = 0, 1, 2, by

$$\beta_{0} := |D_{i-1}^{1} f|^{2} + |\mathbf{p}_{1}(D)_{i-1} f|^{2} = |f_{i} - f_{i-1}|^{2} + |e^{\gamma_{i} \Delta x} f_{i} - f_{i-1}|^{2},
\beta_{1} := |D_{i}^{1} f|^{2} + |\mathbf{p}_{1}(D)_{i} f|^{2} = |f_{i+1} - f_{i}|^{2} + |e^{\gamma_{i+1} \Delta x} f_{i+1} - f_{i}|^{2},
\beta_{2} := \frac{1}{2} (\beta_{1} + (|D_{i+1}^{1} f|^{2} + |\mathbf{p}_{1}(D)_{i+1} f|^{2}))
= \frac{1}{2} (|f_{i+1} - f_{i}|^{2} + |e^{\gamma_{i+1} \Delta x} f_{i+1} - f_{i}|^{2} + |f_{i+2} - f_{i+1}|^{2} + |e^{\gamma_{i+2} \Delta x} f_{i+2} - f_{i+1}|^{2}).$$
(27)

In smooth regions, β_k should be small, so we select the parameter γ_i in a way that depends on the given stencil data:

$$\gamma_{i+\nu} \Delta x = -\frac{f_{i+\nu} - f_{i+\nu-1}}{f_{i+\nu} \delta}, \quad \text{sign}(\delta) := \text{sign}(f_i), \quad \nu \in \{0, 1, 2\},$$
 (28)

where $\delta = \delta(\Delta x)$ is introduced to prevent the denominator from becoming zero. Observe that β_2 is defined using three points (S_2^+ in Fig. 1) instead of two points, which incorporates a bias in the indicators.

Next, using the local smoothness indicators, we map the linear weights d_k to the nonlinear weights α_k for k = 0, 1, 2 via

$$\alpha_k = d_k \left(1 + \frac{\tau}{\beta_k + \varepsilon} + \left(\frac{\beta_k}{\tau + \varepsilon} \right)^2 \right), \quad \varepsilon := \varepsilon(\Delta x), \tag{29}$$

where $\epsilon > 0$ is used to prevent the denominator from becoming zero. Here τ measures the global smoothness and is defined by $\tau = |\beta_2 - \beta_0|$ in WENO-RBF3 and $\tau = |\beta_1 - \beta_0|$ in WENO-RBF4. The linear weights $\{d_k : k = 0, 1, 2\}$ are chosen so that the linear combination of fourth order local approximations, on each of the two-point stencils, is consistent with the sixth order approximation obtained on the four-point stencil by RBF approximation from section 3. Detailed explanation and explicit formula for d_k are given in subsection 5.2. The nonlinear weights for WENO-RBF3 are then scaled to form a partition of unity

$$\omega_k = \frac{\alpha_k}{\sum_{\ell=0}^1 \alpha_\ell}, \quad k = 0, 1 \tag{30}$$

and the nonlinear weights for WENO-RBF4 are defined by

$$\omega_k = \frac{\alpha_k}{\sum_{\ell=0}^2 \alpha_\ell}, \quad k = 0, 1, 2. \tag{31}$$

The value $u_{j+1/2}^-$ is approximated by a convex combination of local approximations over each of the substencils S_k using the nonlinear weights ω_k so that

$$u_{j+1/2}^- := \sum_{k=0}^1 \omega_k u_{j+1/2}^{(k)},$$

and

$$u_{j+1/2}^- := \sum_{k=0}^2 \omega_k u_{j+1/2}^{(k)},$$

in the WENO-RBF3 scheme and WENO-RBF4 scheme, respectively. The analogous construction for $u_{j+1/2}^+$ follows by symmetry. In the next section, we present our full FV WENO-RBF algorithm and some details concerning the implementation.

5. Implementing new WENO-RBF schemes

Now that we have introduced the key components of the proposed schemes (see sections 3 and 4), we can describe the implementation. First, we begin with some details regarding hybrid WENO schemes in section 5.1, before summarizing the key steps of the FV WENO-RBF algorithm in section 5.2. Then, in section 5.3, we briefly discuss the implementation of the proposed schemes to multi-dimensional problems, focusing, in particular on the two-dimensional scalar case. Stencil coefficients for the RBF (Gaussian) methods developed in this work can be found in Appendix B.

5.1. Comments on the hybrid implementation

The implementation of the WENO-RBF4 method used in this work employs a hybrid strategy, which aims to alleviate the computational cost associated with WENO methods due to the additional cost from smoothness indicators and mappings for the nonlinear weights. The basic idea of a hybrid approach is to use reconstructions on a fixed set of cell average data in regions where the data is smooth, while non-smooth regions are appropriately handled with a WENO scheme (see e.g., section 4). The adaptive selection of a reconstruction method relies on the use of certain smoothness criterion, which are, ideally, inexpensive to evaluate. This criterion can, for example, be evaluated with smoothness indicators, such as those in the classical WENO approach [26], as well as divided or undivided differences. A tolerance (or threshold) then selects the reconstruction method according to the smoothness of the given data. Our selection process consists of the following steps:

1. Using finite differences, first compute the relative smoothness $r(x_i)$, which we define as

$$r(x_i) = \frac{2(\left|\delta[\bar{u}](x_i)\right| + \left|\delta^2[\bar{u}](x_i)\right|)}{\left|\Delta^-[\bar{u}](x_{i-1})\right| + \left|\delta^2[\bar{u}](x_{i-1})\right| + \left|\Delta^+[\bar{u}](x_{i+1})\right| + \left|\delta^2[\bar{u}](x_{i+1})\right|}, \quad i = 1, \dots, N,$$
(32)

where δ and δ^2 are central difference operators for first and second derivatives, and Δ^- and Δ^+ are the backward and forward difference operators for the first derivative. These difference approximations are all computed to second order accuracy. Note that along the boundaries, data from an extension is required and can be constructed using extrapolation of sufficient accuracy.

2. Once step 1 is complete, we find the minimum and maximum values of the relative smoothness r_{min} and r_{max} and then compute the tolerance

$$r_{tol} = \min\left(\theta, \kappa \frac{r_{min} + \epsilon}{r_{max} + \epsilon}\right). \tag{33}$$

In the numerical experiments which use the hybrid approach, we take $\theta = 1.5$, $\kappa = 5$, and $\epsilon = 1 \times 10^{-10}$.

3. Next, we map $r(x_i) \mapsto \{0,1\}$ using the previously computed tolerance r_{tol} . We identify cells, which are to use WENO reconstructions, as those for which $r(x_i) \ge r_{tol}$, using fixed stencil reconstructions for those that remain. To account for shortcomings in the definition of the relative smoothness (32), we flag a buffer zone of 4 cells in each direction around any cell marked for WENO reconstruction.

The parameter choices used for θ and κ are based on numerical experimentation and are, by no means, exhaustive. While it is entirely possible that better choices for these parameters exist, it is beyond the scope of this work. Experimentation with different parameters mostly resulted in a more conservative hybrid algorithm, where the WENO reconstruction process was being applied in larger regions of the domain, even where the solution is smooth. While these selections were not particularly detrimental to the shock-capturing abilities of the method, the resulting imbalance does increase the time-to-solution, as the WENO reconstruction is more expensive.

5.2. The FV WENO-RBF component

Once a method for each cell has been selected, the algorithm then applies the corresponding reconstruction technique. The basic steps in the algorithm for the WENO-RBF3 and WENO-RBF4 methods are exactly the same, so we will only present a summary for WENO-RBF4. As discussed in the previous section, cells deemed smooth use a four-point fixed stencil RBF interpolant; regions characterized as "non-smooth" apply the WENO-RBF algorithm, which proceeds as follows:

1. Using (14), form the local approximations $u_{j+1/2}^{(k)}$ on each of the two-point substencils $S_k := \{x_{j+k-1}, x_{j+k}\}$, with k = 0, 1, 2.

$$u_{j+1/2}^{(k)} := \sum_{\ell=0}^{1} c_{\ell}^{k} \bar{u}_{j+k-1+\ell}.$$

The coefficients c_{ℓ}^k , where $\ell=0,1$ and k=0,1,2, are defined with the local shape parameter for the RBF $\phi(x)=\exp(-\lambda_{\ell}^2x^2)$ obtained from (15):

$$\lambda_L^2 \approx -\frac{u''(x_{j+\frac{1}{2}})}{6u(x_{j+\frac{1}{2}})}.$$

Here the function values are replaced with cell averages and the derivatives are obtained with finite differences.

2. Using (19), we can form the approximation $u_{i+1/2}^{S_4}$ on the big stencil $S_4 := \{x_{j-1}, \dots, x_{j+2}\}$ as

$$u_{j+1/2}^{S_4} = \sum_{\ell=-1}^{2} C_{\ell} \bar{u}_{j+\ell},$$

where C_{ℓ} , and $\ell = -1, \dots, 2$ is a coefficient which is dependent on the global shape parameter λ_G . For the RBF $\phi(x) = \exp(-\lambda_G^2 x^2)$, this is reflected in (20):

$$\lambda_G^2 \approx \frac{-\frac{1}{3} u''(x_{j+\frac{1}{2}}) \pm \sqrt{\frac{1}{9} u''(x_{j+\frac{1}{2}})^2 - \frac{1}{15} u(x_{j+\frac{1}{2}}) u^{(4)}(x_{j+\frac{1}{2}})}}{2 u(x_{j+\frac{1}{3}})}.$$

As in step 1, the function values are replaced with cell averages and the derivatives are obtained with finite differences, as described at the end of section 3.1.1.

3. Compute the linear WENO weights $\{d_k : k = 0, 1, 2\}$ which satisfy

$$\sum_{k=0}^{2} d_k u_{j+1/2}^{(k)} = u_{j+1/2}^{S_4} + O(\Delta x^p),$$

using an appropriate high order p from step 1 and step 2. This results in weights of the form

$$d_0 = \frac{C_{-1}}{c_0^0}, \quad d_2 = \frac{C_2}{c_1^2}, \quad d_1 = 1 - d_0 - d_2.$$

This reflects the partition of unity for the linear weights.

- 4. Using the cell averages, compute the parameters (28) and the smoothness indicators (27).
- 5. Map the linear weights $\{d_k : k = 0, 1, 2\}$ from step 3 to nonlinear weights $\{\omega_k : k = 0, 1, 2\}$ using equations (29) and (31).
- 6. Obtain the reconstructed value at the cell interface using the nonlinear weights:

$$u_{j+1/2}^{-} = \sum_{k=0}^{2} \omega_k u_{j+1/2}^{(k)}.$$

The procedure for determining $u_{j+1/2}^+$ follows, analogously, by reflecting the cell average stencil data. Once the reconstructions for $u_{j+1/2}^\pm$ are completed, we simply apply the numerical flux function (24), which yields $\hat{f}_{j+1/2}$. In the case of hyperbolic systems, these reconstructions are performed component-wise on the characteristic variables.

5.3. Extensions for two-dimensional problems

We briefly present, here, an extension of the WENO-RBF3 scheme to two-dimensional scalar conservation laws of the form

$$\begin{cases} u_t + f(u)_x + g(u)_y = 0, & (x, y) \in \mathbb{R} \times \mathbb{R}, \\ u(x, y, 0) = u_0(x, y). \end{cases}$$
(34)

Using the definition of the cell averages of the solution u

$$\bar{u}_{ij} := \bar{u}_{ij}(t) := \frac{1}{\Delta x \Delta y} \int_{x_{i-\frac{1}{2}}}^{x_{i+\frac{1}{2}}} \int_{y_{j-\frac{1}{2}}}^{y_{j+\frac{1}{2}}} u(x, y) \, dy \, dx, \tag{35}$$

we can recast equation (34) in its semi-discrete form, which is given by

$$\frac{d}{dt}\bar{u}_{ij}(t) = -\frac{1}{\Delta x} \left(f_{i+\frac{1}{2},j} - f_{i-\frac{1}{2},j} \right) - \frac{1}{\Delta y} \left(g_{i,j+\frac{1}{2}} - g_{i,j-\frac{1}{2}} \right), \tag{36}$$

where we have defined the fluxes

$$f_{i\pm\frac{1}{2},j} = \frac{1}{\Delta y} \int_{y_{j-\frac{1}{2}}}^{y_{j+\frac{1}{2}}} f\left(u(x_{i\pm\frac{1}{2}}, y)\right) dy,$$

$$g_{i,j\pm\frac{1}{2}} = \frac{1}{\Delta x} \int_{x_{i-\frac{1}{2}}}^{x_{i+\frac{1}{2}}} g\left(u(x, y_{j\pm\frac{1}{2}})\right) dx.$$
(37)

We discuss the construction of the flux $f_{i+\frac{1}{2},j}$ in (37), as the components $f_{i-\frac{1}{2},j}$ and $g_{i,j\pm\frac{1}{2}}$ can be obtained in an analogous manner. The integrals in the flux $f_{i+\frac{1}{2},j}$ can be discretized with numerical quadrature, such as Gaussian quadratures or analytical integration using polynomial interpolation of a specified degree. For this work, we adopt the former approach, and employ Gauss-Legendre quadrature to perform the integration. In either case, with a selection of N integration points $\{y_{\alpha} \in [y_{j-\frac{1}{3}}, y_{j+\frac{1}{3}}] : \alpha = 1, \cdots, N\}$ this leads to a discretization of the form

$$f_{i+\frac{1}{2},j} \approx \frac{1}{\Delta y} \sum_{\alpha=1}^{N} w_{\alpha} f\left(u(x_{i+\frac{1}{2}}, y_{\alpha})\right),\tag{38}$$

with the corresponding integration weights w_{α} for $\alpha=1,\cdots,N$. The flux $f\left(u(x_{i+\frac{1}{2}},y_{\alpha})\right)$ appearing in (38) will be replaced by the numerical flux

$$\hat{f}\left(u_{i+\frac{1}{2},\alpha}^{-},u_{i+\frac{1}{2},\alpha}^{+}\right),\tag{39}$$

where we have used $u_{i+\frac{1}{2},\alpha}^-$ and $u_{i+\frac{1}{2},\alpha}^+$ to denote the left and right states, respectively, which are taken about the interface $x=x_{i+\frac{1}{2}}$, along the integration points y_{α} for $\alpha=1,\cdots,N$.

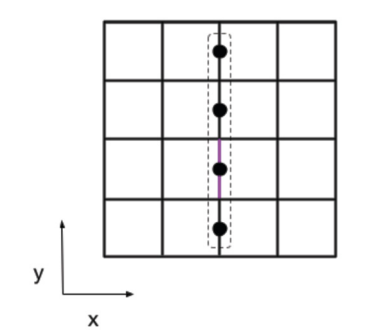
Following Remark 3.2, the WENO-RBF3 scheme requires (for fourth order accuracy) a 4×4 patch of cell averages $\bar{u}_{\ell,m}$, for $\ell=i-1,\cdots,i+2$ and $m=j-1,\cdots,j+2$, to construct $u_{i+\frac{1}{2},\alpha}^-$. First, for each $m=j-1,\cdots,j+2$, using a set of 4 points $\{\bar{u}_{\ell,m}:\ell=i-1,\cdots,i+2\}$, we construct the approximation Av_m^- to the one-dimensional averages of the solution v_m^- with respect to y direction

$$v_{m} = \frac{1}{\Delta y} \int_{y_{m-\frac{1}{2}}}^{y_{m+\frac{1}{2}}} u\left(x_{i\pm\frac{1}{2}}, y\right) dy, \tag{40}$$

by applying the WENO-RBF3 scheme discussed in section 5. Now that we have produced the 4 points $\{Av_m^-: m=j-1,\cdots,j+2\}$, the point-wise values along the quadrature points can be obtained through interpolation. When the data is smooth, we can apply fixed stencil reconstructions at each of the integration points, e.g.,

$$u_{i+\frac{1}{2},\alpha}^{-} = \sum_{m=j-1}^{j+2} L(y_{\alpha}) A v_{m}^{-}, \quad \alpha = 1, \dots, N,$$
(41)

where L(y) is a Lagrange polynomial obtained from the points $\{Av_m^-\}$. In the event that the data is no longer guaranteed to be smooth, we can, instead, use a variant of the WENO-RBF3 scheme to perform the interpolation at quadrature points, rather than equation (41). An diagram of the patch used in the reconstructions for $u_{i+\frac{1}{2},\alpha}^-$ and $u_{\alpha,j+\frac{1}{2}}^-$ is shown in Fig. 2. If WENO schemes are used to perform interpolations at quadrature points, the interpolation coefficients on the substencils



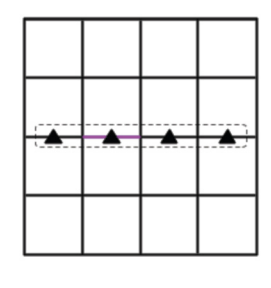


Fig. 2. The 4×4 reconstruction patch used in the fourth order accurate WENO-RBF3 scheme. The first set of WENO reconstructions provides the data indicated by circles and triangles. This data is then used to construct interpolating functions that are projected onto the corresponding quadrature points, which lie on faces of cell (i, j), i.e., $u_{i+\frac{1}{2},\alpha}^-$ (left) and $u_{\alpha,j+\frac{1}{2}}^-$ (right), shown in magenta. We wish to emphasize that the data on remaining faces of cell (i, j) can be reconstructed using this same 4×4 patch of data, since the approximations used in the shape parameter do not have to be properly winded. (For interpretation of the colors in the figure(s), the reader is referred to the web version of this article.)

now depend on the evaluation point, in addition to certain information about the cell in which the reconstructions are performed. Consequently, this also holds for the linear WENO weights $\{d_k\}$, which may cause (some of) the linear weights to become negative [36]. For this reason, a more systematic treatment of multi-dimensional problems shall be deferred to future work, where we shall consider alternative formulations that avoid the issue of negative weights [6]. Instead, the developments provided in this work will employ fixed stencil reconstructions, such as (41), at the quadrature points.

6. Numerical results

In this section, we provide some experimental results that demonstrate the improvements offered by the non-polynomial basis. We begin by observing the numerical convergence order of proposed schemes for the scalar advection equation. Then we investigate the performance of the proposed methods on some one-dimensional benchmark problems for the Euler equations before testing the method on the more challenging pressureless Euler system, which is weakly hyperbolic. All test problems use a third order explicit strong-stability preserving Runge-Kutta method [14] for time integration. In our experiments, we compute the cell average values, from the initial conditions, using high-order Gauss-Legendre quadrature. We compare the proposed methods, which are labeled as WENO-RBF3 and WENO-RBF4, with third order and fifth order classical WENO schemes [26] and WENO-Z schemes [5]. These are labeled as WENO-JS3/WENO-Z3 and WENO-JS5/WENO-Z5, respectively. We also compare WENO-RBF3 with third order WENO scheme proposing a new smoothness indicator [17], labeling as WENO-NZ3, for selected meaningful examples. Unless otherwise stated, the results for the WENO-RBF4 scheme used a second order approximation (i.e., p=2) for the shape parameter (20). Lastly, note that the implementation of the WENO-RBF4 method uses the hybrid strategy discussed in section 5.1.

6.1. Scalar problems for convergence rates

We consider the linear equation

$$u_t + u_x = 0, \quad x \in [-1, 1],$$

with periodic boundary condition. To find the approximation order of the proposed methods for the numerical problems without and with critical points, the experiments are performed with two initial functions $u(x, t = 0) = \sin(\pi x)$ and $u(x, t = 0) = \sin^4(\pi x)$. In Table 2, for the smooth initial condition $\sin(\pi x)$, the proposed RBF schemes achieve clear desired order of accuracy. For the initial function $\sin^4(\pi x)$ which contains a critical point where the first derivative vanishes but second derivative does not, the WENO-RBF3 scheme is degenerated to the clear third order in the presence of a critical point with smaller errors than WENO-Z3. The reason is easily verifiable that the tension parameter used for the RBF3 scheme given in (16) has the first derivative information so that it cannot be applied to enhance the order of accuracy. However, it is noticeable that WENO-RBF4 achieves stable sixth order of convergence even near the critical points.

6.2. Hyperbolic system

We now present numerical results for the one-dimensional Euler equations of gas dynamics

$$U_t + F(U)_x = 0,$$
 (42)

where V and F(V) are given as

Table 2 L_{∞} and L_1 errors and convergence rates (*) at t=2.

		$u(x,0) = \sin(\pi x)$		$\sin^4(\pi x)$	
L_{∞}	N _x	WENO-Z3	RBF3 (Proposed)	WENO-Z3	RBF3 (Proposed
	20	7.01e-02 (–)	2.24e-03 (-)	4.57e-01 (-)	2.14e-01 (-)
	40	1.65e-02 (2.08)	1.85e-04 (3.59)	1.90e-01 (1.27)	5.79e-02 (1.88
	80	3.64e-03 (2.18)	1.72e-05 (3.43)	3.66e-02 (2.38)	8.66e-03 (2.74
	160	7.96e-04 (2.19)	2.59e-06 (2.73)	8.32e-03 (2.14)	1.11e-03 (2.96
	320	1.68e-04 (2.25)	2.70e-07 (3.26)	1.79e-03 (2.21)	1.39e-04 (2.99
L_1	N_{x}	WENO-Z3	RBF3 (Proposed)	WENO-Z3	RBF3 (Proposed
	20	4.61e-02 (-)	6.39e-04 (-)	2.13e-01 (-)	9.21e-02 (-)
	40	6.98e-03 (2.72)	5.30e-05 (3.59)	8.07e-02 (1.40)	3.02e-02 (1.61
	80	9.69e-04 (2.85)	4.22e-06 (3.65)	1.74e-02 (2.21)	4.53e-03 (2.74
	160	1.28e-04 (2.92)	3.08e-07 (3.77)	2.56e-03 (2.76)	5.86e-04 (2.95
	320	1.65e-05 (2.96)	2.36e-08 (3.71)	3.40e-04 (2.91)	7.36e-05 (3.00
		$u(x,0) = \sin(\pi x)$		$\sin^4(\pi x)$	
L_{∞}	N_x	WENO-Z5	RBF4 (Proposed II)	WENO-Z5	RBF4 (Proposed I
	20	3.42e-04 (-)	5.13e-04 (-)	1.07e-01 (-)	4.24e-02 (-)
	40	1.02e-05 (5.07)	8.26e-06 (5.96)	5.65e-03 (4.24)	1.42e-03 (4.90)
	80	3.14e-07 (5.02)	1.29e-07 (6.00)	3.71e-04 (3.93)	2.52e-05 (5.81)
	160	9.79e-09 (5.00)	2.02e-09 (6.00)	4.80e-05 (2.95)	4.08e-07 (5.95)
	320	3.06e-10 (5.00)	3.42e-11 (5.89)	4.36e-06 (3.46)	6.27e-09 (6.02)
L_1	N_x	WENO-Z5	RBF4 (Proposed II)	WENO-Z5	RBF4 (Proposed I
	20	2.06e-04 (-)	1.57e-04 (–)	5.80e-02 (-)	2.74e-02 (-)
	40	6.24e-06 (5.05)	2.55e-06 (5.94)	2.62e-03 (4.47)	6.31e-04 (5.44)
	80	1.97e-07 (4.99)	4.05e-08 (5.98)	1.65e-04 (3.99)	1.04e-05 (5.92)
	160	6.19e-09 (4.99)	6.36e-10 (5.99)	8.83e-06 (4.22)	1.59e-07 (6.03)
	320	1.94e-10 (5.00)	1.15e-11 (5.79)	4.09e-07 (4.43)	2.48e-09 (6.01)

$$U = (\rho, \rho u, E)^{T},$$

 $F(U) = (\rho u, \rho u^{2} + p, u(E + p))^{T}.$

Here ρ , p, u and E are the density, pressure, velocity, and total energy, respectively. Additionally, we use the equation of state

$$p = (\gamma - 1)(E - \frac{1}{2}\rho u^2), \quad c = \sqrt{\frac{\gamma p}{\rho}},$$

with $\gamma = 1.4$. Here, c denotes the local speed of sound in the gas.

All test problems for the hyperbolic system use the HLLC Riemann solver [43] to compute the flux. Following [22], the HLLC flux is of the form

$$h(U_l, U_r)^T = \begin{cases} F(U_l), & \text{if } s^- \ge 0, \\ F_l^*, & \text{if } s^* \ge 0 \ge s^-, \\ F_r^*, & \text{if } s^+ \ge 0 \ge s^*, \\ F(U_r), & \text{if } s^+ < 0, \end{cases}$$

$$(43)$$

where the intermediate velocity is defined as

$$s^* = \frac{p_r - p_l + \rho_l u_l (s^- - u_l) - \rho_r u_r (s^+ - u_r)}{\rho_l (s^- - u_l) - \rho_r (s^+ - u_r)}.$$

Estimates for the minimum and maximum wave speeds given, respectively, by

$$s^- = \min(u_l - c_l, u_l, u_l + c_l), \quad s^+ = \min(u_r - c_r, u_r, u_r + c_r).$$

Using the Roe pressure

$$p_{lr} = \frac{p_r + p_l + \rho_l(s^- - u_l)(s^* - u_l) + \rho_r(s^* - u_r)(s^+ - u_r)}{2},$$

we form the intermediate fluxes F_i^* and F_r^*

$$F_{l}^{*} = \frac{s^{*} \left(s^{-} u_{l} - F(U_{l}) \right) + s^{-} p_{lr} \left(0, 1, s^{*} \right)^{T}}{s^{-} - s^{*}}, \quad F_{r}^{*} = \frac{s^{*} \left(s^{+} u_{r} - F(U_{r}) \right) + s^{-} p_{lr} \left(0, 1, s^{*} \right)^{T}}{s^{+} - s^{*}}.$$

Table 3 (Example 6.1) L_{∞} and L_1 errors and convergence rates (*) at t=1.

-				
L_{∞}	N _x	WENO-JS3	WENO-Z3	RBF3 (Proposed)
	20	3.04e-01 (-)	2.78e-01 (-)	1.66e-02 (-)
	40	1.57e-01 (0.96)	8.59e-02 (1.69)	6.01e-04 (4.79)
	80	4.81e-02 (1.71)	2.78e-02 (1.63)	2.06e-05 (4.87)
	160	1.58e-02 (1.61)	4.66e-03 (2.58)	8.06e-07 (4.68)
	320	2.80e-03 (2.50)	4.45e-04 (3.39)	7.75e-08 (3.38)
L_1	N_{x}	WENO-JS3	WENO-Z3	RBF3 (Proposed)
	20	4.73e-01 (-)	4.38e-01 (-)	2.67e-02 (-)
	40	2.79e-01 (0.76)	1.87e-01 (1.23)	1.08e-03 (4.63)
	80	1.11e-01 (1.33)	6.38e-02 (1.55)	3.60e-05 (4.90)
	160	4.19e-02 (1.41)	1.78e-02 (1.85)	1.28e-06 (4.82)
	320	1.22e-02 (1.78)	3.09e-03 (2.52)	1.25e-07 (3.35)
L_{∞}	N_{x}	WENO-JS5	RBF4 (Proposed I)	RBF4 (Proposed II)
	20	1.17e-02 (–)	3.12e-03 (-)	3.03e-04 (-)
	40	6.95e-04 (4.07)	1.02e-04 (4.94)	5.70e-06 (5.73)
	80	2.61e-05 (4.74)	3.21e-06 (4.99)	8.71e-08 (6.03)
	160	8.70e-07 (4.91)	1.00e-07 (5.00)	1.39e-09 (5.97)
	320	2.68e-08 (5.02)	3.14e-09 (5.00)	2.16e-11 (6.01)
L_1	N_{x}	WENO-JS5	RBF4 (Proposed I)	RBF4 (Proposed II)
	20	8.14e-03 (-)	1.60e-03 (-)	1.61e-04 (-)
	40	3.74e-04 (4.45)	5.29e-05 (4.92)	3.31e-06 (5.61)
	80	1.18e-05 (4.98)	1.68e-06 (4.98)	5.31e-08 (5.96)
	160	3.69e-07 (5.00)	5.27e-08 (5.00)	8.39e-10 (5.98)
	320	1.15e-08 (5.00)	1.65e-09 (5.00)	1.31e-11 (6.00)

Example 6.1. First, we consider the smooth advection problem. Using the initial data

$$\rho(x) = 1 + 0.5 \sin(4\pi x)$$
,

along with the selections u = 1, and p = 1, the system reduces to a single advection equation, subject to periodic boundary conditions. The exact solution on [0, 1] is given by

$$\rho(x,t) = 1 + 0.5 \sin\left(4\pi \left(x - ut\right)\right).$$

In Table 3, we present both the numerical errors and convergence orders of the proposed scheme. When setting the shape parameter λ^2 for the RBF $\phi = e^{-\lambda^2 x^2}$, the approximations in (20) were computed to first and second order accuracy (i.e., p=1 and 2 in (20)). These choices are reflected under the respective labels "Proposed I" and "Proposed II" shown in Table 3. The results demonstrate the expected improved convergence through the choice of the shape parameter. With regard to the three-point methods, the proposed RBF scheme achieves its intended accuracy along with a noticeable reduction in the errors compared to alternative reconstruction methods.

Example 6.2. We test our method using the Lax problem [27] with the initial condition

$$(\rho, u, p) = \begin{cases} (0.445, 0.698, 3.528) & \text{if } x \in [-5, 0), \\ (0.50, 0, 0.571) & \text{if } x \in [0, 5]. \end{cases}$$

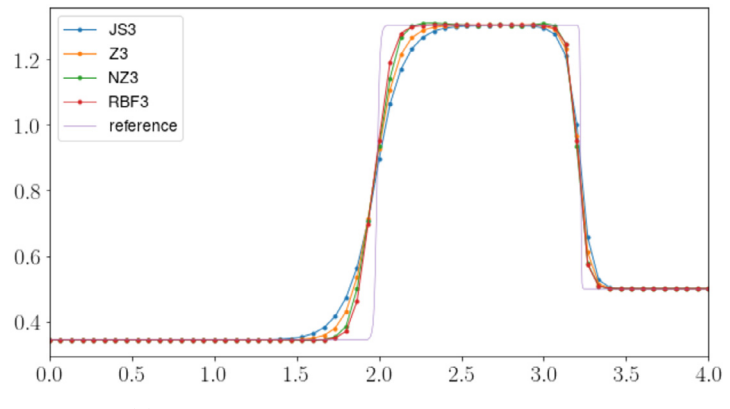
The numerical results for the density profiles are displayed in Fig. 3, at time t = 1.3, using $\Delta x = 10/200$.

Among three-point WENO schemes, the proposed method demonstrates improvement in capturing the jumps in the profile, when compared to other three-point WENO methods. In the case of the four-point RBF schemes, the method provides improvements over WENO-JS and is comparable to the solution generated with WENO-Z5. This similarity may be a consequence of the size of the substencils employed by each of the methods. The substencils used in WENO-JS5 and WENO-Z5 consist of three points, whereas the proposed four-point RBF methods use substencils with two points. This discrepancy in the behavior of the method is something we wish to address in a subsequent paper.

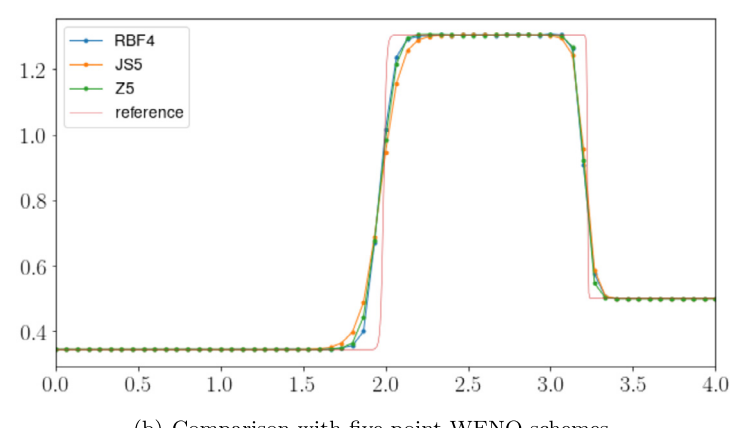
Example 6.3. As a next example, let us consider the Sod problem [40] with the initial condition

$$(\rho,u,p) = \begin{cases} (1.000,0.750,1.000) & \text{if } x \in [0,0.5), \\ (0.125,0.000,0.100) & \text{if } x \in [0.5,1]. \end{cases}$$

The numerical results for density profiles are given in Fig. 4 at time t = 0.2 using $\Delta x = 1/100$. Here, we observe results which are similar to the Lax problem (see Example 6.2). As noted above, we plan to investigate these shortcomings in our future work involving WENO-RBF methods.



(a) Comparison of three-point WENO schemes.



(b) Comparison with five-point WENO schemes.

Fig. 3. (Example 6.2) Density profiles of Lax problem [27] at t = 1.3 with $\Delta x = 10/150$.

Example 6.4. We now look at the Shu-Osher problem [38], which uses Riemann initial data for the shock entropy wave interaction. The approximate solutions are computed on the interval [–5, 5] with the initial state

$$(\rho, u, p) = \begin{cases} (3.857143, 2.629369, 10.33333) & \text{if } x \in [-5, -4), \\ (1 + \varepsilon \sin(kx), 0, 1) & \text{if } x \in [-4, 5], \end{cases}$$

$$(44)$$

where k and ε denote the wave number and amplitude of the entropy wave respectively. We take k=5 and $\varepsilon=0.2$ in our experiments.

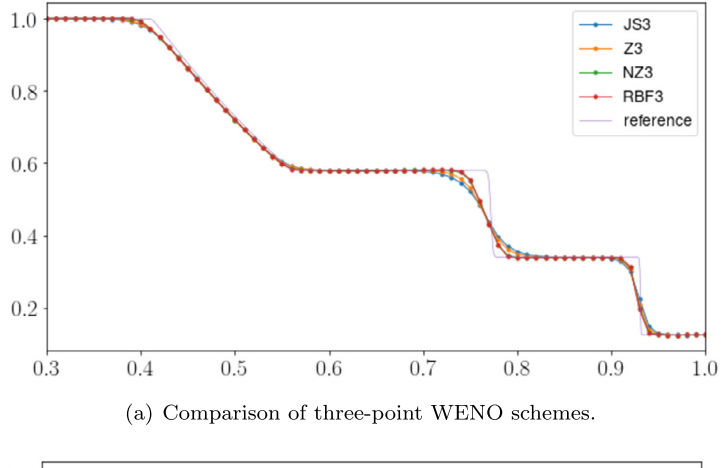
In Fig. 5, we provide plots which compare the proposed WENO-RBF methods against three-point and five-point WENO methods. We observe the largest improvement in the comparison of three-point WENO schemes, with the WENO-RBF3 method producing results with less dissipation than WENO-JS3 and WENO-Z3. With regard to the four-point method, i.e., WENO-RBF4, improvements over WENO-JS5 are quite clear. These improvements are less apparent when compared against WENO-Z5, which seems to perform better in certain areas. As discussed in Example 6.2, part of this improvement may be attributed to the larger substencil size used by the WENO-Z5 method.

Example 6.5. In [42], Titarev and Toro suggested the following Riemann initial data for the shock entropy wave interaction:

$$(\rho, u, p) = \begin{cases} (1.515695, 0.523346, 1.80500) & \text{if } x \in [-5, -4.5), \\ (1 + 0.1\sin(20\pi x), 0, 1) & \text{if } x \in [-4.5, 5], \end{cases}$$

on the interval [-5, 5]. Fig. 6 shows the results for this test case at time at t = 5. This problem allows us to test the method in environments that support highly oscillatory structures. Compared to the Shu-Osher problem (see Example 6.4), the prescribed initial density exhibits a much larger wave number, i.e., 20.

Among the three-point WENO schemes, we see from Fig. 6(a) that the WENO-RBF3 method offers a clear improvement over WENO-JS3 and WENO-Z3. We also find that WENO-RB4 yields an improvement over the results obtained for the Shu-Osher problem, with regard to capturing complex wave patterns. While there is a clear improvement in capturing the



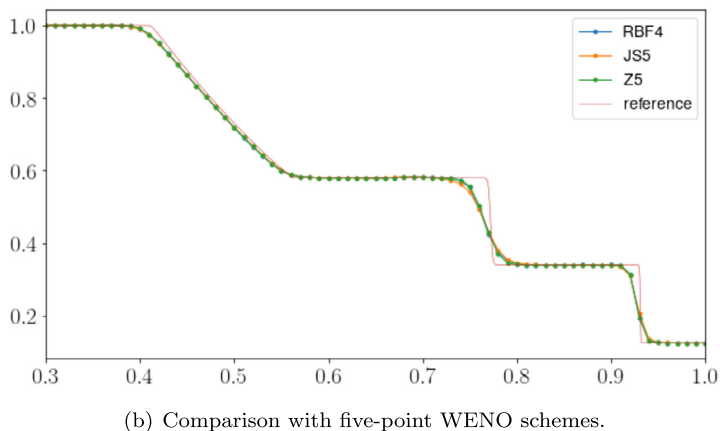


Fig. 4. (Example 6.3) Density profiles of Sod problem [40] at t = 0.2 using $\Delta x = 1/100$.

features of the small wavelength oscillations, we do note the slight undershoot and overshoot in the vicinity of x = -1.9, where the transition into the oscillatory region occurs. This behavior is far less apparent in the WENO-JS5 and WENO-Z5 methods.

6.3. Weakly hyperbolic system

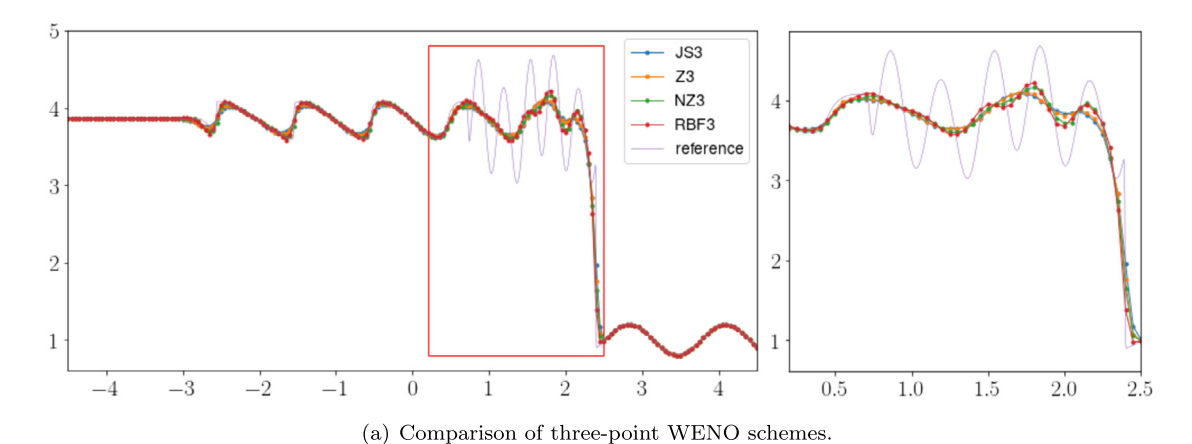
In this subsection, we consider the more challenging pressureless Euler system, which, in one space dimension, is given by

$$U_t + F(U)_x = 0, (45)$$

with

$$U = (\rho, \rho u)^T$$
, $F(U) = (\rho u, \rho u^2)^T$.

The system (45) is important in modeling systems of dilute gases in a vacuum which undergo few collision events. When collisions do occur, they are said to be perfectly inelastic, which causes the gas particles to stick together. These collisions lead to the emergence of so-called δ -shocks, which are the primary feature of interest in these models. Note that because the system is weakly hyperbolic, the characteristic decomposition is not available for this problem. Consequently, the simple Lax-Friedrichs flux cannot be directly used in this problem. Instead, we consider the Godunov flux, outlined in [46], which was originally introduced by Bouchut, *et al.*[7]. Before defining the flux, we remark that the latter work contains a fairly diverse collection of literature on isothermal gas dynamics, so we refer the interested reader to references therein for further details. The former article considered more general problems involving δ -shocks, including the system (45), and applied DG methods to solve such problems. To define the flux, suppose we have left and right numerical approximations $U_1 = (\rho_1, \rho_1 u_1)^T$ and $U_r = (\rho_r, \rho_r u_r)^T$. Then, the numerical flux is given by



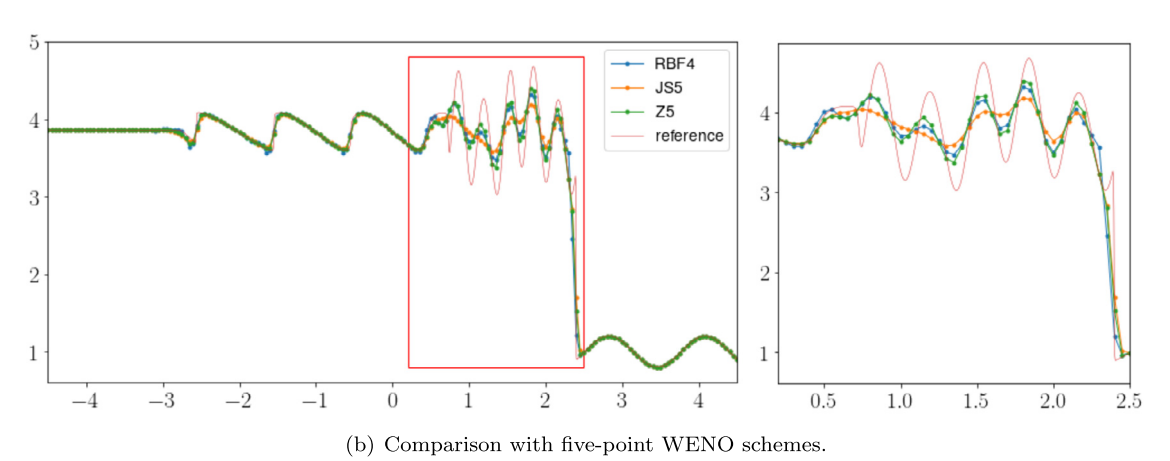


Fig. 5. (Example 6.4) Density profiles of the shock-entropy interaction problem at t = 1.8, with $\Delta x = 10/300$.

$$h(U_{l}, U_{r})^{T} = \begin{cases} \left(\rho_{l}u_{l}, \rho_{l}u_{l}^{2}\right)^{T}, & \text{if } u_{l} > 0, u_{r} > 0, \\ \left(0, 0\right)^{T}, & \text{if } u_{l} \leq 0, u_{r} > 0, \\ \left(\rho_{r}u_{r}, \rho_{r}u_{r}^{2}\right)^{T}, & \text{if } u_{l} \leq 0, u_{r} \leq 0, \\ \left(\rho_{l}u_{l}, \rho_{l}u_{l}^{2}\right)^{T}, & \text{if } u_{l} > 0, u_{r} \leq 0, v > 0, \\ \left(\rho_{r}u_{r}, \rho_{r}u_{r}^{2}\right)^{T}, & \text{if } u_{l} > 0, u_{r} \leq 0, v < 0, \\ \left(\frac{\rho_{l}u_{l} + \rho_{r}u_{r}}{2}, \rho_{l}u_{l}^{2} = \rho_{r}u_{r}^{2}\right)^{T}, & \text{if } u_{l} > 0, u_{r} \leq 0, v = 0, \end{cases}$$

where

$$v = \frac{\sqrt{\rho_l}u_l + \sqrt{\rho_r}u_r}{\sqrt{\rho_l} + \sqrt{\rho_r}}.$$

Example 6.6. For our first test, we seek to determine the approximation order for the weak hyperbolic system. To this end, we solve pressureless Euler system (45) with the following initial data

$$\rho_0(x) = \sin(x) + 2$$
, $u_0(x) = \sin(x) + 2$,

subject to periodic boundary conditions. The exact solution for this problem is

$$\rho(x,t) = \frac{\rho_0(x_0)}{1 + tu_0'(x_0)}, \quad u(x,t) = u_0(x_0),$$

where x_0 is given implicitly by

$$x_0 + tu_0(x_0) = x.$$

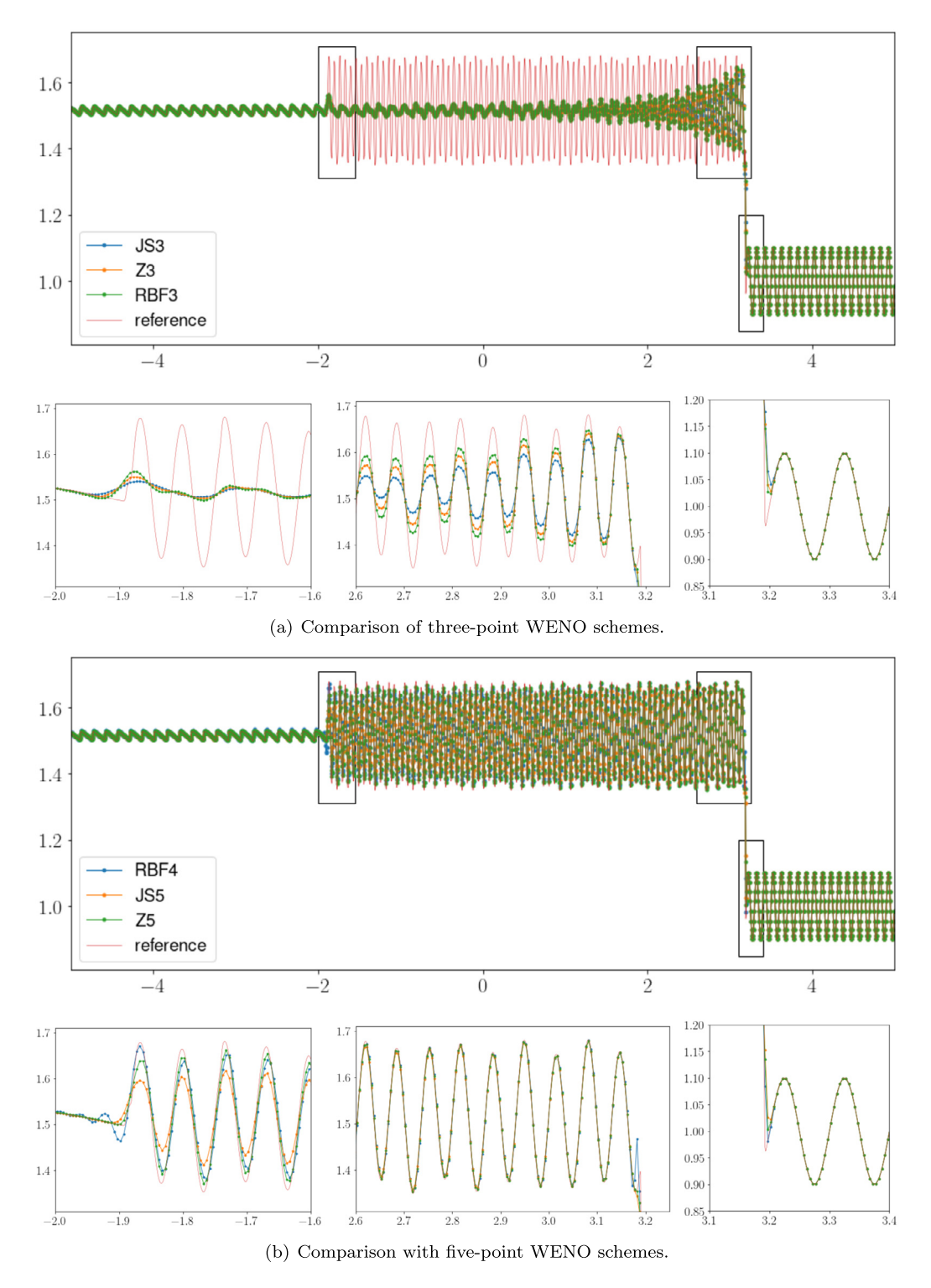


Fig. 6. (Example 6.5) Density profiles of the shock-turbulence problem [42] at t = 5 using $\Delta x = 1/200$.

The L_{∞} and L_1 errors and approximation orders for the density ρ at t=0.1 are given in Table 4. For the three-point methods, we find that both WENO-JS3 and WENO-Z3 exhibit difficulties in achieving second order accuracy. While some reduction in the error is attained by switching from WENO-JS3 to WENO-Z3, we find that convergence properties are fairly similar between these two methods. In contrast, the WENO-RBF3 method achieves the intended convergence rate along with significant reduction in the error.

Table 4 (Example 6.6) L_{∞} and L_1 errors and convergence rates (*) at t=0.1.

-		-		
L_{∞}	N _x	WENO-JS3	WENO-Z3	RBF3 (Proposed)
	20	6.27e-02 (-)	6.16e-02 (-)	7.87e-03 (–)
	40	6.20e-02 (0.02)	4.86e-02 (0.34)	3.96e-03 (0.99)
	80	1.26e-01 (-1.03)	5.82e-02 (-0.26)	3.19e-04 (3.64)
	160	3.15e-02 (2.00)	1.68e-02 (1.79)	2.06e-05 (3.95)
	320	1.66e-02 (0.93)	5.50e-03 (1.62)	1.22e-06 (4.08)
L_1	N_{x}	WENO-JS3	WENO-Z3	RBF3 (Proposed)
	20	8.88e-02 (-)	8.16e-02 (-)	1.64e-02 (-)
	40	3.97e-02 (1.16)	2.83e-02 (1.53)	6.91e-03 (1.25)
	80	4.46e-02 (-0.16)	1.42e-02 (0.99)	5.37e-04 (3.69)
	160	9.68e-03 (2.20)	5.41e-03 (1.39)	3.39e-05 (3.98)
	320	2.81e-03 (1.78)	8.37e-04 (2.69)	2.21e-06 (3.94)
L_{∞}	N_{x}	WENO-JS5	RBF4 (Proposed I)	RBF4 (Proposed II)
	20	1.89e-03 (-)	8.38e-04 (-)	7.38e-04 (–)
	40	6.90e-05 (4.77)	1.98e-05 (5.41)	1.32e-05 (5.80)
	80	3.62e-06 (4.25)	5.68e-07 (5.12)	2.12e-07 (5.96)
	160	2.48e-07 (3.87)	1.67e-08 (5.08)	3.37e-09 (5.97)
	320	1.90e-08 (3.71)	5.05e-10 (5.05)	5.30e-11 (5.99)
L_1	N_{x}	WENO-JS5	RBF4 (Proposed I)	RBF4 (Proposed II)
	20	3.23e-03 (–)	1.95e-03 (–)	1.45e-03 (-)
	40	1.13e-04 (4.84)	4.52e-05 (5.43)	2.41e-05 (5.91)
	80	3.68e-06 (4.94)	1.15e-06 (5.30)	3.81e-07 (5.98)
	160	1.25e-07 (4.88)	3.17e-08 (5.17)	6.04e-09 (5.98)
			9.27e-10 (5.10)	9.47e-11 (5.99)

Similarly, in the case of the four-point method (WENO-RBF4), we achieve the intended accuracy of the method. In accordance with Theorem 3.3, the shape parameters for the RBF $\phi = e^{-\lambda^2 x^2}$, were computed to first and second order accuracy (i.e., p=1 and p=2 in (20)) and have been assigned the corresponding labels "Proposed I" and "Proposed II", as in the Example 6.1. Moreover, these schemes exhibit convergence rates, of fifth and sixth order accuracy, respectively, as shown in Table 4. In contrast, the WENO-JS5 scheme suffers a reduction in the convergence order by nearly a factor of two, a feature which was also observed in [46].

Example 6.7. We solve the problem known as two interactive blast wave problem [44] which has the initial data

$$(\rho_0, u_0) = \begin{cases} (1, 1) & \text{if } x < 0, \\ (0.25, 0) & \text{if } x > 0. \end{cases}$$

In Fig. 7, we plot the density profiles for each of the methods at time t = 0.3.

Our results indicate that the three-point WENO methods provide fairly similar estimates of the shock width, but produce remarkable differences in the overall height of the δ -shock, as shown in Fig. 7(a). Of these methods, the shock generated by WENO-RBF3 method exhibits the sharpest peak, compared to WENO-JS3 and WENO-Z3. Similar observations can be made regarding the four-point WENO-RBF4 method, which is presented in Fig. 7(b). The shock width predicted by the WENO-RBF4 method is, again, sharper and slightly more narrow than the that predicted by WENO-JS5 and WENO-Z5. To the right of the shock, we also observe some undershoots in the densities predicted by each of these methods; however, the undershoot in the RBF method is marginally smaller than WENO-JS5 and noticeably smaller than WENO-Z5. As discussed earlier, reducing the overshoot and undershoot in these rapidly varying transition regions is something we plan to address in our future work.

6.4. Two-dimensional scalar hyperbolic problem

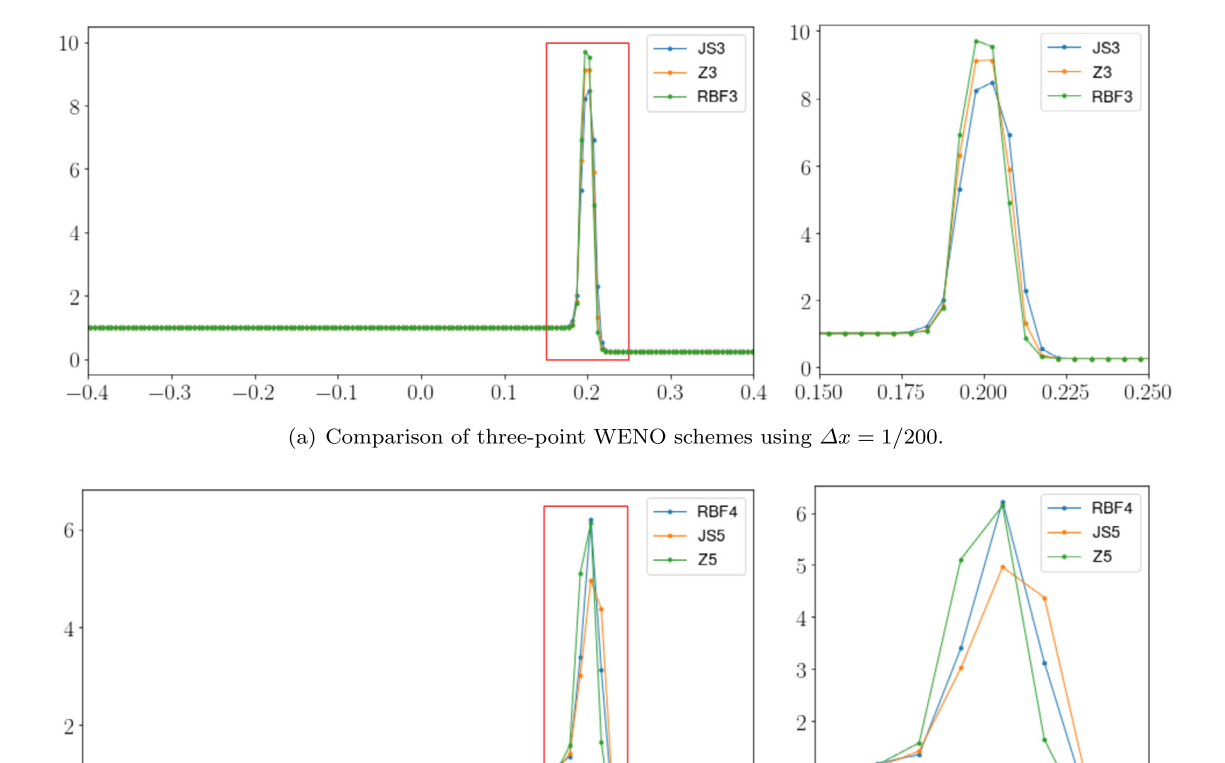
In this section, we present convergence results for a two-dimensional scalar problem using the extensions described in section 5.3. As discussed earlier, an extension to multi-dimensional problems can be achieved with line-by-line applications of the proposed one-dimensional WENO schemes, introduced earlier in this work (see e.g., section 4). We only provide results for a single two-dimension test problem, as a proof of concept, since this is not the central theme of this paper. In a subsequent article, we plan to focus our efforts on two and three-dimensional applications.

Example 6.8. In this example, we apply the three-point RBF scheme to a multi-dimensional problem, focusing, in particular, on the two-dimensional Burgers' equation

0.225

0.250

0.200



(b) Comparison with five-point WENO schemes using $\Delta x = 1/80$.

0.3

0.150

0.175

0.4

0.2

Fig. 7. (Example 6.7) Density profiles of δ -shock wave problem [44] at t = 0.3.

$$u_t + \frac{1}{2} (u^2)_x + \frac{1}{2} (u^2)_y = 0.$$

-0.3

-0.4

-0.2

-0.1

0.0

0.1

We use the initial condition

$$u(x, 0) = 0.5 + \sin(x + y),$$

along with periodic boundary conditions on the domain $[-\pi,\pi] \times [-\pi,\pi]$. For this problem, we used the local Lax-Friedrichs flux

$$h(u^{-}, u^{+}) = \frac{f(u^{-}) + f(u^{+})}{2} - \alpha \frac{u^{+} - u^{-}}{2}, \tag{46}$$

where α is the maximum wave speed taken over the local states

$$\alpha = \max(|u^-|, |u^+|).$$

Convergence of the smooth solutions was measured using the final time T=0.2 and we chose the timestep size according to $\Delta t=\min(\Delta x^{4/3},\Delta y^{4/3})$. We report the L_{∞} and L_1 errors and convergence rates in Table 5 for each of the three-point WENO schemes. In each of these methods, we used the same fifth order Lagrange interpolating polynomial (41) to perform the reconstructions at the quadrature points.

Our preliminary results indicate that the WENO-RBF3 method achieves, at least, third order accuracy and with the convergence rate tending to fourth order as the mesh resolution increases. Moreover, the errors in the proposed scheme, when compared to WENO-JS3 and WENO-Z3, are noticeably smaller. Given that each of these methods used the same quadrature reconstruction procedure, this improvement stems from the use of the new reconstruction method. We note that the convergence rates for the WENO-RBF3 method, in this example, are not ideal, which is something we are currently working to resolve.

Table 5 (Example 6.8) L_{∞} and L_1 errors and convergence rates (*) at t = 0.2.

L_{∞}	$N_x \times N_y$	WENO-JS3	WENO-Z3	RBF3
	10 × 10	8.2958e-02 (-)	6.9456e-02 (-)	1.9902e-02 (-)
	20×20	4.5343e-02 (0.87)	3.7121e-02 (0.90)	1.1847e-02 (0.75)
	40×40	1.9416e-02 (1.22)	1.4812e-02 (1.33)	2.2575e-03 (2.39)
	80×80	7.7397e-03 (1.33)	4.9918e-03 (1.57)	2.6275e-04 (3.10)
	160×160	2.5147e-03 (1.62)	9.7351e-04 (2.36)	2.0994e-05 (3.65)
L ₁	$N_{x} \times N_{y}$	WENO-IS3	WENO-Z3	RBF3
- 1	1 V $\chi \wedge 1$ V y	WENO-JSS	WLINO-25	CIGN
-1	$\frac{N_x \times N_y}{10 \times 10}$	1.2567e+00 (-)	1.0833e+00 (-)	3.0803e-01 (-)
-1		<u> </u>		
-1	10 × 10	1.2567e+00 (-)	1.0833e+00 (-)	3.0803e-01 (-)
-1	10 × 10 20 × 20	1.2567e+00 (-) 4.2019e-01 (1.58)	1.0833e+00 (-) 2.8167e-01 (1.94)	3.0803e-01 (-) 9.6608e-02 (1.67)

7. Conclusion

In this paper, we proposed several FV WENO-RBF methods which achieve enhanced order of convergence using a non-polynomial basis consisting of RBFs. Order enhancing in the interpolation component of the reconstruction was achieved by exploiting the shape parameter in the definition of the RBF basis. By analyzing the error in the reconstructions, we derived expressions for optimal shape parameters which improved the convergence order of the interpolation. While the methods developed in this work considered Gaussian RBFs, the same techniques can be easily applied (or adapted) to develop schemes using other non-polynomial FV methods. The proposed schemes, which make use of fairly compact stencils, incorporate new smoothness indicators that were previously shown to be highly effective at discerning rapid changes in a function, even on a small data stencils. To alleviate the heavy computational cost typically associated with WENO methods, we also implemented a hybrid solver that dynamically prescribes the reconstruction method according to the local smoothness of the function.

The proposed schemes were compared with several well-known methods using one-dimensional systems of conservation laws, along with a two-dimensional test problem to demonstrate extensions to multiple dimensions. While the proposed methods demonstrated improved shock-capturing capabilities, the use of the non-polynomial basis was shown to be particularly effective for problems exhibiting rapid transitions as well as complex wave structures and singularities. A notable contribution of this work was the development of a genuinely third order WENO scheme, which could be promoted to fourth order accuracy with minimal additional computational expense. Furthermore, in the case of the pressureless Euler equations, the proposed WENO-RBF methods were experimentally shown to achieve their theoretical convergence rates, avoiding the order reduction encountered by competitive reconstruction techniques. A highlight of this work is reflected in the blast wave problem (see Example 6.7 in section 6.3), where the proposed RBF methods lead to markedly different predictions of the shock. While these results suggest several avenues for future research, we plan to conduct additional experiments to develop multi-dimensional algorithms and investigate strategies for further reducing oscillations surrounding transition regions and singularities.

CRediT authorship contribution statement

- Andrew Christlieb:
 - Conceptualization, Methodology, Supervision, Project administration
- Hyoseon Yang:
 - Conceptualization, Methodology, Software, Formal analysis, Writing
- William Sands:
 - Methodology, Software, Investigation, Writing, Visualization

Declaration of competing interest

The authors declare that they have no known competing financial interests or personal relationships that could have appeared to influence the work reported in this paper.

Data availability

No data was used for the research described in the article.

Acknowledgements

We would like to thank Air Force Office of Scientific Research and National Science Foundation for their support of this work under grants FA9550-19-1-0281 and FA9550-17-1-0394 and DMS 1912183. Also this work was supported by a grant

from Kyung Hee University in 2021 (KHU-20211822) and by the National Research Foundation of Korea (NRF) grant funded by the Korea government(MSIT) (No. 2022R1F1A1066389).

Appendix A. Approximating the shape parameter λ^2

We briefly describe the procedure used to compute the optimal shape parameter λ^2 in the radial basis function $\phi(x) = \exp(-\lambda^2 x^2)$. In this example, we consider the (fixed stencil) RBF3 scheme with the shape parameter defined in (16), and we assume a set of cell average values $\{\bar{u}_k\}$ is available.

To obtain the interface values $u_{j+1/2}^-$ and $u_{j+1/2}^+$, the reconstruction stencils are given, respectively, as $\{\bar{u}_{j-1}, \bar{u}_{j}, \bar{u}_{j+1}\}$ and $\{\bar{u}_{j}, \bar{u}_{j+1}, \bar{u}_{j+2}\}$. The base method, ignoring the optimal selection of λ^2 , reconstructs $u_{j+1/2}^-$ and $u_{j+1/2}^+$ using a three-point stencil of cell averages. Hence, in order to compute the numerical flux at the cell boundary $x_{j+1/2}$, we require a total of four cell averages: $\{\bar{u}_{j-1}, \bar{u}_{j}, \bar{u}_{j+1}, \bar{u}_{j+2}\}$; however, we show, below, that this same set of points can be used to approximate the optimal value of λ^2 , which promotes the approximation from third to fourth order accuracy. While it may appear that the method requires an additional point, the effective stencil is identical to the one generated by the third order WENO-JS scheme. In other words, no additional points are required beyond what is already needed for the analogous classical scheme.

If we represent the cell average values using Taylor expansion, then it follows that we can obtain the linear combination of cell averages \bar{u}_k which approximate $u'''(x_{j+\frac{1}{2}})$ and $u'(x_{j+\frac{1}{2}})$, i.e., the derivatives of the function at the cell boundary $x_{j+\frac{1}{2}}$, as follows:

$$u'(x_{j+\frac{1}{2}}) = \frac{1}{\Delta x} \left(\frac{1}{12} \bar{u}_{j-1} - \frac{5}{4} \bar{u}_{j} + \frac{5}{4} \bar{u}_{j+1} - \frac{1}{12} \bar{u}_{j+2} \right) + \mathcal{O}(\Delta x^{3}),$$

$$u'''(x_{j+\frac{1}{2}}) = \frac{1}{\Delta x^{3}} \left(-\bar{u}_{j-1} + 3\bar{u}_{j} - 3\bar{u}_{j+1} + \bar{u}_{j+2} \right) + \mathcal{O}(\Delta x).$$

We remark that because the shape parameter is used to promote the accuracy of the reconstructions in smooth regions, these difference approximations for the derivative do not need to account for wind-direction. Using these approximations, can compute the shape parameter

$$\begin{split} \lambda^2 &= -\frac{-\bar{u}_{j-1} + 3\bar{u}_j - 3\bar{u}_{j+1} + \bar{u}_{j+2}}{\Delta x^2 \left(\bar{u}_{j-1} - 15\bar{u}_j + 15\bar{u}_{j+1} - \bar{u}_{j+2}\right)},\\ &= -\frac{u'''(x_{j+\frac{1}{2}})}{12u'(x_{j+\frac{1}{2}})} + \mathcal{O}(\Delta x), \end{split}$$

which meets the convergence criteria, shown in equation (16), that is required to promote the reconstruction to fourth order accuracy. In order to prevent a division by zero, in regions where the function data is "flat", we instead use

$$u'(x_{j+\frac{1}{2}}) \approx \frac{1}{\Delta x} \left(\frac{1}{12} \bar{u}_{j-1} - \frac{5}{4} \bar{u}_j + \frac{5}{4} \bar{u}_{j+1} - \frac{1}{12} \bar{u}_{j+2} \right) + \varepsilon, \quad \varepsilon := \varepsilon(\Delta x),$$

with ε having the same sign as the first group of terms involving differences of the cell average data.

Appendix B. Stencil coefficients for the WENO-RBF methods

This section provides the stencil coefficients used by the WENO-RBF schemes presented in this work, which assume the basis function is a Gaussian (see section 3). We treat the shape parameter(s), i.e., λ^2 , as input in the reconstruction procedure. For simplicity, we present the expressions using a single shape parameter, but, in general, each (sub)stencil may be associated with its own shape parameter. An example calculation, for the shape parameter, in the fixed-stencil RBF3 scheme, is provided in Appendix A.

B.1. Three-point scheme

Using the global stencil of cell-averages $S_3 := \{\bar{u}_{j-1}, \bar{u}_j, \bar{u}_{j+1}\}$ one obtains, following the procedure in section 3, the fixed stencil reconstruction of the form

$$u_{j+1/2}^{S_3} = C_{-1}\bar{u}_{j-1} + C_0\bar{u}_j + C_1\bar{u}_{j+1}.$$

To improve the efficiency of the method and simplify the implementation of the method, we chose to Taylor expand the expressions coefficients (up to the order of the global stencil), which results in the following:

$$\begin{split} C_{-1} &= -\frac{1}{6} - \frac{1}{3} \lambda^2 \Delta x^2 + \left(\lambda^2 \Delta x^2\right)^2 - \frac{5}{9} \left(\lambda^2 \Delta x^2\right)^3, \\ C_0 &= \frac{5}{6} - \frac{1}{3} \lambda^2 \Delta x^2 + \frac{5}{6} \left(\lambda^2 \Delta x^2\right)^2 - \frac{5}{9} \left(\lambda^2 \Delta x^2\right)^3, \\ C_1 &= \frac{1}{3} - \frac{2}{3} \lambda^2 \Delta x^2 + \frac{1}{6} \left(\lambda^2 \Delta x^2\right)^2 - \frac{5}{9} \left(\lambda^2 \Delta x^2\right)^3. \end{split}$$

Similarly, using the two-point substencils $S_0 := \{\bar{u}_{j-1}, \bar{u}_j\}$ and $S_1 := \{\bar{u}_j, \bar{u}_{j+1}\}$, one obtains the reconstructions

$$u_{j+1/2}^{(0)} = c_0^0 \bar{u}_{j-1} + c_1^0 \bar{u}_{j},$$

$$u_{j+1/2}^{(1)} = c_0^1 \bar{u}_j + c_1^1 \bar{u}_{j+1},$$

with the corresponding (expanded) coefficients given by

$$\begin{split} c_0^0 &= -\frac{1}{2} - \frac{2}{3} \left(\lambda^2 \Delta x^2 \right)^2 + \left(\lambda^2 \Delta x^2 \right)^3, \\ c_1^0 &= \frac{3}{2} - 2\lambda^2 \Delta x^2 + \left(\lambda^2 \Delta x^2 \right)^2, \\ c_0^1 &= \frac{1}{2} + \frac{1}{2} \lambda^2 \Delta x^2 - \frac{1}{12} \left(\lambda^2 \Delta x^2 \right)^2 - \frac{1}{4} \left(\lambda^2 \Delta x^2 \right)^3, \\ c_1^1 &= \frac{1}{2} + \frac{1}{2} \lambda^2 \Delta x^2 - \frac{1}{12} \left(\lambda^2 \Delta x^2 \right)^2 - \frac{1}{4} \left(\lambda^2 \Delta x^2 \right)^3. \end{split}$$

B.2. Four-point scheme

Using the global stencil of cell-averages $S_4 := \{\bar{u}_{j-1}, \cdots, \bar{u}_{j+2}\}$ one obtains, following the procedure in section 3, the fixed stencil reconstruction of the form

$$u_{j+1/2}^{S_4} = C_{-1}\bar{u}_{j-1} + C_0\bar{u}_j + C_1\bar{u}_{j+1} + C_2\bar{u}_{j+2}$$

Performing Taylor expansions on the set coefficients, as in Appendix B.1, we obtain

$$\begin{split} C_{-1} &= -\frac{1}{12} - \frac{1}{3}\lambda^2 \Delta x^2 - \frac{1}{3} \left(\lambda^2 \Delta x^2\right)^2 + \frac{4}{9} \left(\lambda^2 \Delta x^2\right)^4, \\ C_0 &= \frac{7}{12} + \frac{1}{3}\lambda^2 \Delta x^2 - \frac{2}{3} \left(\lambda^2 \Delta x^2\right)^2 - \frac{1}{9} \left(\lambda^2 \Delta x^2\right)^4, \\ C_1 &= \frac{7}{12} + \frac{1}{3}\lambda^2 \Delta x^2 - \frac{2}{3} \left(\lambda^2 \Delta x^2\right)^2 - \frac{1}{9} \left(\lambda^2 \Delta x^2\right)^4, \\ C_2 &= -\frac{1}{12} - \frac{1}{3}\lambda^2 \Delta x^2 - \frac{1}{3} \left(\lambda^2 \Delta x^2\right)^2 + \frac{4}{9} \left(\lambda^2 \Delta x^2\right)^4. \end{split}$$

On each of the two-point substencils $S_0 := \{\bar{u}_{j-1}, \bar{u}_j\}$, $S_1 := \{\bar{u}_j, \bar{u}_{j+1}\}$, and $S_2 := \{\bar{u}_{j+1}, \bar{u}_{j+2}\}$, one obtains the reconstructions

$$u_{j+1/2}^{(0)} = c_0^0 \bar{u}_{j-1} + c_1^0 \bar{u}_j,$$

$$u_{j+1/2}^{(1)} = c_0^1 \bar{u}_j + c_1^1 \bar{u}_{j+1},$$

$$u_{j+1/2}^{(2)} = c_0^2 \bar{u}_{j+1} + c_1^2 \bar{u}_{j+2},$$

with the corresponding (expanded) coefficients given by

$$\begin{split} c_0^0 &= -\frac{1}{2} - \frac{2}{3} \left(\lambda^2 \Delta x^2 \right)^2 + \left(\lambda^2 \Delta x^2 \right)^3 - \frac{103}{180} \left(\lambda^2 \Delta x^2 \right)^4, \\ c_1^0 &= \frac{3}{2} - 2\lambda^2 \Delta x^2 + \left(\lambda^2 \Delta x^2 \right)^2 - \frac{1}{5} \left(\lambda^2 \Delta x^2 \right)^4, \\ c_0^1 &= \frac{1}{2} + \frac{1}{2} \lambda^2 \Delta x^2 - \frac{1}{12} \left(\lambda^2 \Delta x^2 \right)^2 - \frac{1}{4} \left(\lambda^2 \Delta x^2 \right)^3 + \frac{7}{720} \left(\lambda^2 \Delta x^2 \right)^4, \\ c_1^1 &= \frac{1}{2} + \frac{1}{2} \lambda^2 \Delta x^2 - \frac{1}{12} \left(\lambda^2 \Delta x^2 \right)^2 - \frac{1}{4} \left(\lambda^2 \Delta x^2 \right)^3 + \frac{7}{720} \left(\lambda^2 \Delta x^2 \right)^4, \\ c_0^2 &= \frac{3}{2} - 2\lambda^2 \Delta x^2 + 2 \left(\lambda^2 \Delta x^2 \right)^2 - \left(\lambda^2 \Delta x^2 \right)^3 + \frac{13}{60} \left(\lambda^2 \Delta x^2 \right)^4, \end{split}$$

$$c_1^2 = -\frac{1}{2} + \frac{1}{3} \left(\lambda^2 \Delta x^2 \right)^2 - \frac{7}{45} \left(\lambda^2 \Delta x^2 \right)^4.$$

References

- [1] F. Acker, R.B. de, R. Borges, B. Costa, An improved WENO-Z scheme, J. Comput. Phys. 313 (2016) 726-753.
- [2] S. Adjerid, K.D. Devine, J.E. Flaherty, L. Krivodonova, A posteriori error estimation for discontinuous Galerkin solutions of hyperbolic problems, Comput. Methods Appl. Mech. Eng. 191 (2002) 1097–1112.
- [3] S. Adjerid, T.C. Massey, Superconvergence of discontinuous Galerkin solutions for a nonlinear scalar hyperbolic problem, Comput. Methods Appl. Mech. Eng. 195 (2006) 3331–3346.
- [4] C. Bigoni, J.S. Hesthaven, Adaptive WENO methods based on radial basis function reconstruction, J. Sci. Comput. 72 (2017) 986-6020.
- [5] R. Borges, M. Carmona, B. Costa, W.S. Don, An improved WENO scheme for hyperbolic conservation laws, I. Comput. Phys, 227 (2008) 3191-3211.
- [6] P. Buchmüller, C. Helzel, Improved accuracy of high-order WENO finite volume methods on Cartesian grids, J. Sci. Comput. 61 (2014) 343-368.
- [7] F. Bouchut, S. Jin, X. Li, Numerical approximations of pressureless and isothermal gas dynamics, SIAM J. Numer. Anal. 41 (2003) 135–158.
- [8] M.D. Buhmann, Radial basis functions, Acta Numer. 9 (2000) 1-38.
- [9] W. Cao, Z. Zhang, Q. Zou, Superconvergence of discontinuous Galerkin methods for linear hyperbolic equations, SIAM J. Numer. Anal. 52 (2014) 2555–2573.
- [10] Y. Cheng, C. Shu, Superconvergence and time evolution of discontinuous Galerkin finite element solutions, J. Comput. Phys. 227 (2008) 9612-9627.
- [11] Y. Cheng, C. Shu, Superconvergence of discontinuous Galerkin and local discontinuous Galerkin schemes for linear hyperbolic and convection-diffusion equations in one space dimension, SIAM J. Numer. Anal. 47 (2010) 4044–4072.
- [12] D. Gottlieb, C.-W. Shu, On the Gibbs phenomenon and its resolution, SIAM Rev. 39 (4) (1997) 644-668,
- [13] D. Gottlieb, C.-W. Shu, A. Solomonoff, H. Vandeven, On the Gibbs phenomenon I: recovering exponential accuracy from the Fourier partial sum of a nonperiodic analytic function, J. Comput. Appl. Math. 43 (1992) 81–98.
- [14] S. Gottlieb, C.W. Shu, E. Tadmor, Strong stability-preserving high-order time discretization methods, SIAM Rev. 43 (2001) 89-112.
- [15] J. Guo, J.-H. Jung, A RBF-WENO finite volume method for hyperbolic conservation laws with the monotone polynomial interpolation method, Appl. Numer. Math. 112 (2017) 27–50.
- [16] Y. Ha, C.H. Kim, Y.H. Yang, J. Yoon, Sixth-order weighted essentially non-oscillatory schemes based on exponential polynomials, SIAM J. Sci. Comput. 38 (4) (2016) A1987–A2017.
- [17] Y. Ha, C.H. Kim, Y.H. Yang, J. Yoon, Construction of an improved third-order WENO scheme with a new smoothness indicator, J. Sci. Comput. 82 (2020) 63.
- [18] Y. Ha, C.H. Kim, Y.H. Yang, J. Yoon, Improving accuracy of the fifth-order WENO scheme by using the exponential approximation space, preprint, arXiv:2002.06175, 2020.
- [19] A. Harten, S. Osher, Uniformly high-order accurate non-oscillatory schemes I, SIAM J. Numer. Anal. 24 (2) (1987) 279-309.
- [20] A. Harten, B. Engquist, S. Osher, S. Chakravarthy, Uniformly high-order accurate non-oscillatory schemes III, J. Comput. Phys. 131 (1997) 3-47.
- [21] A.K. Henrick, T.D. Aslam, J.M. Powers, Mapped weighted-essentially-non-oscillatory schemes: achieving optimal order near critical points, J. Comput. Phys. 207 (2005) 542–567.
- [22] J.S. Hesthaven, Numerical methods for conservation laws: from analysis to algorithms, SIAM Comput. Sci. Eng. (2018).
- [23] J.S. Hesthaven, F. ö Monkeberg, Entropy stable essentially nonoscillatory methods based on RBF reconstruction, ESAIM: Math. Model. Numer. Anal. 53 (3) (2019) 925–958
- [24] J.S. Hesthaven, F. ö Monkeberg, Two-dimensional RBF-ENO method on unstructured grids, J. Sci. Comput. 82 (3) (2020) 1–24.
- [25] J.S. Hesthaven, F. ö Monkeberg, Two-dimensional RBF-ENO method on unstructured grids, J. Sci. Comput. 12 (2021) 100089 (32 pp.).
- [26] G. Jiang, C.W. Shu, Efficient implementation of weighted ENO schemes, J. Comput. Phys. 126 (1996) 202-228.
- [27] P.D. Lax, Weak solutions of nonlinear hyperbolic equations and their numerical computation, Commun. Pure Appl. Math. 7 (1954) 159-193.
- [28] X.-D. Liu, S. Osher, T. Chan, Weighted essentially non-oscillatory schemes, I. Comput. Phys. 115 (1994) 200–212.
- [29] S.E. Olson, A.J. Christlieb, Gridless DSMC, J. Comput. Phys. 227 (2008) 8035–8064.
- [30] A. Reyes, D. Lee, C. Graziani, P. Tzeferacos, A new class of high-order methods for fluid dynamics simulations using Gaussian process modeling, J. Sci. Comput. 76 (2018) 443–480.
- [31] A. Reyes, D. Lee, C. Graziani, P. Tzeferacos, A variable high-order shock-capturing finite difference method with GP-WENO, J. Comput. Phys. 381 (2019) 189–217.
- [32] J. Ryan, C.W. Shu, On a one-sided post-processing technique for the discontinuous Galerkin methods, Methods Appl. Anal. 10 (2003) 295-308.
- [33] J. Ryan, C.W. Shu, H. Atkins, Extension of a post processing technique for the discontinuous Galerkin method for hyperbolic equations with application to an aeroacoustic problem, SIAM J. Sci. Comput. 26 (2005) 821–843.
- [34] S.A. Sarra, E.J. Kansa, Multiquadric radial basis function approximation methods for the numerical solution of partial differential equations, Adv. Comput. Mech. 2 (2009).
- [35] S. Serna, A. Marquina, Power-ENO methods: a fifth-order accurate weighted power ENO method, J. Comput. Phys. 194 (2004) 632–658.
- [36] J. Shi, C. Hu, C.W. Shu, A technique of treating negative weights in WENO schemes, J. Comput. Phys. 175 (2002) 108-127.
- [37] C.-W. Shu, S. Osher, Efficient implementation of essentially non-oscillatory shock capturing schemes, J. Comput. Phys. 77 (1988) 439-471.
- [38] C.-W. Shu, S. Osher, Efficient implementation of essentially non-oscillatory shock capturing schemes II, J. Comput. Phys. 83 (1989) 32–78.
- [39] C.-W. Shu, P.S. Wong, A note on the accuracy of spectral method applied to nonlinear conservation laws, J. Sci. Comput. 10 (3) (1995) 357–369.
- [40] G. Sod, A survey of several finite difference methods for systems of nonlinear hyperbolic conservation laws, J. Comput. Phys. 27 (1978) 1-31.
- [41] T. Sonar, Optimal recovery using thin plate splines in finite volume methods for the numerical solution of hyperbolic conservation laws, IMA J. Numer. Anal. 16 (4) (1996) 549–981.
- [42] V.A. Titarev, E.F. Toro, Finite-volume WENO schemes for three-dimensional conservation laws, J. Comput. Phys. 201 (2004) 238-260.
- [43] E.F. Toro, Riemann Solvers and Numerical Methods for Fluid Dynamics, Springer-Verlag, New York, 1997.
- [44] P. Woodward, P. Colella, The numerical simulation of two-dimensional fluid flow with strong shocks, J. Comput. Phys. 54 (1984) 115-173.
- [45] Y. Yang, C.W. Shu, Analysis of optimal superconvergence of discontinuous Galerkin method for linear hyperbolic equations, SIAM J. Numer. Anal. 50 (2012) 3110–3133.
- [46] Y. Yang, D. Wei, C.W. Shu, Discontinuous Galerkin method for Krause's consensus models and pressureless Euler equations, J. Comput. Phys. 252 (2013) 109–127
- [47] J. Yoon, Spectral approximation orders of radial basis function interpolation on the sobolev space, SIAM J. Math. Anal. 33 (4) (2001) 946–958.
- [48] J. Zhu, J. Qiu, Trigonometric WENO schemes for hyperbolic conservation laws and highly oscillatory problems, Commun. Comput. Phys. 8 (2010) 1242–1263.
- [49] J. Zhu, J. Qiu, WENO schemes and their application as limiters for RKDG methods based on Trigonometric approximation spaces, J. Sci. Comput. 55 (2013) 606–644.